

Measurement of the τ Michel parameters $\bar{\eta}$ and $\xi\kappa$ in the radiative leptonic decay $\tau^- \rightarrow \ell^- \nu_\tau \bar{\nu}_\ell \gamma$

N. Shimizu¹, H. Aihara¹, D. Epifanov^{2,3}, I. Adachi^{4,5}, S. Al Said^{6,7}, D. M. Asner⁸, V. Aulchenko^{2,3}, T. Aushev⁹, R. Ayad⁶, V. Babu¹⁰, I. Badhrees^{6,11}, A. M. Bakich¹², V. Bansal⁸, E. Barberio¹³, V. Bhardwaj¹⁴, B. Bhuyan¹⁵, J. Biswal¹⁶, A. Bobrov^{2,3}, A. Bozek¹⁷, M. Bračko^{18,16}, T. E. Browder¹⁹, D. Červenkov²⁰, M.-C. Chang²¹, P. Chang²², V. Chekelian²³, A. Chen²⁴, B. G. Cheon²⁵, K. Chilikin^{26,27}, K. Cho²⁸, S.-K. Choi²⁹, Y. Choi³⁰, D. Cinabro³¹, T. Czank³², N. Dash³³, S. Di Carlo³¹, Z. Doležal²⁰, D. Dutta¹⁰, S. Eidelman^{2,3}, J. E. Fast⁸, T. Ferber³⁴, B. G. Fulsom⁸, R. Garg³⁵, V. Gaur³⁶, N. Gabyshev^{2,3}, A. Garmash^{2,3}, M. Gelb³⁷, P. Goldenzweig³⁷, D. Greenwald³⁸, E. Guido³⁹, J. Haba^{4,5}, K. Hayasaka⁴⁰, H. Hayashii⁴¹, M. T. Hedges¹⁹, S. Hirose⁴², W.-S. Hou²², T. Iijima^{43,42}, K. Inami⁴², G. Inguglia³⁴, A. Ishikawa³², R. Itoh^{4,5}, M. Iwasaki⁴⁴, I. Jaegle⁴⁵, H. B. Jeon⁴⁶, S. Jia⁴⁷, Y. Jin¹, K. K. Joo⁴⁸, T. Julius¹³, K. H. Kang⁴⁶, G. Karyan³⁴, T. Kawasaki⁴⁰, C. Kiesling²³, D. Y. Kim⁴⁹, J. B. Kim⁵⁰, S. H. Kim²⁵, Y. J. Kim²⁸, K. Kinoshita⁵¹, P. Kodyš²⁰, S. Korpar^{18,16}, D. Kotchetkov¹⁹, P. Križan^{52,16}, R. Kroeger⁵³, P. Krokovny^{2,3}, R. Kulasiri⁵⁴, A. Kuzmin^{2,3}, Y.-J. Kwon⁵⁵, J. S. Lange⁵⁶, I. S. Lee²⁵, L. K. Li⁵⁷, Y. Li³⁶, L. Li Gioi²³, J. Libby⁵⁸, D. Liventsev^{36,4}, M. Masuda⁵⁹, M. Merola⁶⁰, K. Miyabayashi⁴¹, H. Miyata⁴⁰, G. B. Mohanty¹⁰, H. K. Moon⁵⁰, T. Mori⁴², R. Mussa³⁹, E. Nakano⁴⁴, M. Nakao^{4,5}, T. Nanut¹⁶, K. J. Nath¹⁵, Z. Natkaniec¹⁷, M. Nayak^{31,4}, M. Niiyama⁶¹, N. K. Nisar⁶², S. Nishida^{4,5}, S. Ogawa⁶³, S. Okuno⁶⁴, H. Ono^{65,40}, G. Pakhlova^{26,9}, B. Pal⁵¹, C. W. Park³⁰, H. Park⁴⁶, S. Paul³⁸, T. K. Pedlar⁶⁶, R. Pestotnik¹⁶, L. E. Piilonen³⁶, V. Popov⁹, M. Ritter⁶⁷, A. Rostomyan³⁴, Y. Sakai^{4,5}, M. Salehi^{68,67}, S. Sandilya⁵¹, Y. Sato⁴², V. Savinov⁶², O. Schneider⁶⁹, G. Schnell^{70,71}, C. Schwanda⁷², Y. Seino⁴⁰, K. Senyo⁷³, M. E. Seviour¹³, V. Shebalin^{2,3}, T.-A. Shibata⁷⁴, J.-G. Shiu²², B. Shwartz^{2,3}, A. Sokolov⁷⁵, E. Solovieva^{26,9}, M. Starič¹⁶, J. F. Strube⁸, K. Sumisawa^{4,5}, T. Sumiyoshi⁷⁶, U. Tamponi^{39,77}, K. Tanida⁷⁸, F. Tenchini¹³, K. Trabelsi^{4,5}, M. Uchida⁷⁴, T. Uglov^{26,9}, Y. Unno²⁵, S. Uno^{4,5}, Y. Usov^{2,3}, C. Van Hulse⁷⁰, G. Varner¹⁹, V. Vorobyev^{2,3}, A. Vossen⁷⁹, C. H. Wang⁸⁰, M.-Z. Wang²², P. Wang⁵⁷, M. Watanabe⁴⁰, E. Widmann⁸¹, E. Won⁵⁰, Y. Yamashita⁶⁵, H. Ye³⁴, C. Z. Yuan⁵⁷, Z. P. Zhang⁸², V. Zhilich^{2,3}, V. Zhukova^{26,27}, V. Zhulanov^{2,3}, and A. Zupanc^{52,16}

¹Department of Physics, University of Tokyo, Tokyo 113-0033, Japan

²Budker Institute of Nuclear Physics SB RAS, Novosibirsk 630090, Russia

³Novosibirsk State University, Novosibirsk 630090, Russia

⁴High Energy Accelerator Research Organization (KEK), Tsukuba 305-0801, Japan

⁵SOKENDAI (The Graduate University for Advanced Studies), Hayama 240-0193, Japan

⁶Department of Physics, Faculty of Science, University of Tabuk, Tabuk 71451, Saudi Arabia

⁷Department of Physics, Faculty of Science, King Abdulaziz University, Jeddah 21589, Saudi Arabia

⁸Pacific Northwest National Laboratory, Richland, Washington 99352, USA

⁹Moscow Institute of Physics and Technology, Moscow Region 141700, Russia

¹⁰Tata Institute of Fundamental Research, Mumbai 400005, India

¹¹King Abdulaziz City for Science and Technology, Riyadh 11442, Saudi Arabia

¹²School of Physics, University of Sydney, New South Wales 2006, Australia

¹³School of Physics, University of Melbourne, Victoria 3010, Australia

¹⁴Indian Institute of Science Education and Research Mohali, SAS Nagar, 140306, India

¹⁵Indian Institute of Technology Guwahati, Assam 781039, India

- ¹⁶*J. Stefan Institute, 1000 Ljubljana, Slovenia*
- ¹⁷*H. Niewodniczanski Institute of Nuclear Physics, Krakow 31-342, Poland*
- ¹⁸*University of Maribor, 2000 Maribor, Slovenia*
- ¹⁹*University of Hawaii, Honolulu, Hawaii 96822, USA*
- ²⁰*Faculty of Mathematics and Physics, Charles University, 121 16 Prague, Czech Republic*
- ²¹*Department of Physics, Fu Jen Catholic University, Taipei 24205, RoC*
- ²²*Department of Physics, National Taiwan University, Taipei 10617, RoC*
- ²³*Max-Planck-Institut für Physik, 80805 München, Germany*
- ²⁴*National Central University, Chung-li 32054, RoC*
- ²⁵*Hanyang University, Seoul 133-791, South Korea*
- ²⁶*P.N. Lebedev Physical Institute of the Russian Academy of Sciences, Moscow 119991, Russia*
- ²⁷*Moscow Physical Engineering Institute, Moscow 115409, Russia*
- ²⁸*Korea Institute of Science and Technology Information, Daejeon 305-806, South Korea*
- ²⁹*Gyeongsang National University, Chinju 660-701, South Korea*
- ³⁰*Sungkyunkwan University, Suwon 440-746, South Korea*
- ³¹*Wayne State University, Detroit, Michigan 48202, USA*
- ³²*Department of Physics, Tohoku University, Sendai 980-8578, Japan*
- ³³*Indian Institute of Technology Bhubaneswar, Satya Nagar 751007, India*
- ³⁴*Deutsches Elektronen-Synchrotron, 22607 Hamburg, Germany*
- ³⁵*Panjab University, Chandigarh 160014, India*
- ³⁶*Virginia Polytechnic Institute and State University, Blacksburg, Virginia 24061, USA*
- ³⁷*Institut für Experimentelle Kernphysik, Karlsruher Institut für Technologie, 76131 Karlsruhe, Germany*
- ³⁸*Department of Physics, Technische Universität München, 85748 Garching, Germany*
- ³⁹*INFN - Sezione di Torino, 10125 Torino, Italy*
- ⁴⁰*Niigata University, Niigata 950-2181, Japan*
- ⁴¹*Nara Women's University, Nara 630-8506, Japan*
- ⁴²*Graduate School of Science, Nagoya University, Nagoya 464-8602, Japan*
- ⁴³*Kobayashi-Maskawa Institute, Nagoya University, Nagoya 464-8602, Japan*
- ⁴⁴*Osaka City University, Osaka 558-8585, Japan*
- ⁴⁵*University of Florida, Gainesville, Florida 32611, USA*
- ⁴⁶*Kyungpook National University, Daegu 702-701, South Korea*
- ⁴⁷*Beihang University, Beijing 100191, PRC*
- ⁴⁸*Chonnam National University, Kwangju 660-701, South Korea*
- ⁴⁹*Soongsil University, Seoul 156-743, South Korea*
- ⁵⁰*Korea University, Seoul 136-713, South Korea*
- ⁵¹*University of Cincinnati, Cincinnati, Ohio 45221, USA*
- ⁵²*Faculty of Mathematics and Physics, University of Ljubljana, 1000 Ljubljana, Slovenia*
- ⁵³*University of Mississippi, University, Mississippi 38677, USA*
- ⁵⁴*Kennesaw State University, Kennesaw, Georgia 30144, USA*
- ⁵⁵*Yonsei University, Seoul 120-749, South Korea*
- ⁵⁶*Justus-Liebig-Universität Gießen, 35392 Gießen, Germany*
- ⁵⁷*Institute of High Energy Physics, Chinese Academy of Sciences, Beijing 100049, PRC*
- ⁵⁸*Indian Institute of Technology Madras, Chennai 600036, India*
- ⁵⁹*Earthquake Research Institute, University of Tokyo, Tokyo 113-0032, Japan*
- ⁶⁰*INFN - Sezione di Napoli, 80126 Napoli, Italy*
- ⁶¹*Kyoto University, Kyoto 606-8502, Japan*
- ⁶²*University of Pittsburgh, Pittsburgh, Pennsylvania 15260, USA*
- ⁶³*Toho University, Funabashi 274-8510, Japan*
- ⁶⁴*Kanagawa University, Yokohama 221-8686, Japan*
- ⁶⁵*Nippon Dental University, Niigata 951-8580, Japan*
- ⁶⁶*Luther College, Decorah, Iowa 52101, USA*
- ⁶⁷*Ludwig Maximilians University, 80539 Munich, Germany*
- ⁶⁸*University of Malaya, 50603 Kuala Lumpur, Malaysia*
- ⁶⁹*École Polytechnique Fédérale de Lausanne (EPFL), Lausanne 1015, Switzerland*

- ⁷⁰University of the Basque Country UPV/EHU, 48080 Bilbao, Spain
- ⁷¹IKERBASQUE, Basque Foundation for Science, 48013 Bilbao, Spain
- ⁷²Institute of High Energy Physics, Vienna 1050, Austria
- ⁷³Yamagata University, Yamagata 990-8560, Japan
- ⁷⁴Tokyo Institute of Technology, Tokyo 152-8550, Japan
- ⁷⁵Institute for High Energy Physics, Protvino 142281, Russia
- ⁷⁶Tokyo Metropolitan University, Tokyo 192-0397, Japan
- ⁷⁷University of Torino, 10124 Torino, Italy
- ⁷⁸Advanced Science Research Center, Japan Atomic Energy Agency, Naka 319-1195, Japan
- ⁷⁹Indiana University, Bloomington, Indiana 47408, USA
- ⁸⁰National United University, Miao Li 36003, RoC
- ⁸¹Stefan Meyer Institute for Subatomic Physics, Vienna 1090, Austria
- ⁸²University of Science and Technology of China, Hefei 230026, PRC

Received September 26, 2017; Revised December 28, 2017; Accepted December 28, 2017; Published February 24, 2018

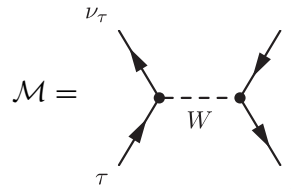
.....
 We present a measurement of the Michel parameters of the τ lepton, $\bar{\eta}$ and $\xi\kappa$, in the radiative leptonic decay $\tau^- \rightarrow \ell^- \nu_\tau \bar{\nu}_\ell \gamma$ using 711 fb^{-1} of collision data collected with the Belle detector at the KEKB e^+e^- collider. The Michel parameters are measured in an unbinned maximum likelihood fit to the kinematic distribution of $e^+e^- \rightarrow \tau^+\tau^- \rightarrow (\pi^+\pi^0\bar{\nu}_\tau)(\ell^-\nu_\tau\bar{\nu}_\ell\gamma)$ ($\ell = e$ or μ). The measured values of the Michel parameters are $\bar{\eta} = -1.3 \pm 1.5 \pm 0.8$ and $\xi\kappa = 0.5 \pm 0.4 \pm 0.2$, where the first error is statistical and the second is systematic. This is the first measurement of these parameters. These results are consistent with the Standard Model predictions within their uncertainties, and constrain the coupling constants of the generalized weak interaction.

Subject Index C01, C07, C21

1. Introduction

In the Standard Model (SM), there are three flavors of charged leptons: e , μ , and τ . The SM has proven to be the fundamental theory in describing the physics of particles; nevertheless, precision tests may reveal the presence of physics beyond the Standard Model (BSM). In particular, a measurement of Michel parameters in leptonic and radiative leptonic τ decays is a powerful probe for the BSM contributions [1,2].

The most general Lorentz-invariant derivative-free matrix element of leptonic τ decay $\tau^- \rightarrow \ell^- \nu_\tau \bar{\nu}_\ell$ ¹ is represented as [3]



$$\mathcal{M} = \begin{array}{c} \nu_\tau \\ \nearrow \\ \bullet \\ \nwarrow \\ \tau \end{array} \text{---} W \text{---} \begin{array}{c} \nu_\ell \\ \nearrow \\ \bullet \\ \nwarrow \\ \ell \end{array} = \frac{4G_F}{\sqrt{2}} \sum_{\substack{N=S,V,T \\ ij=L,R}} g_{ij}^N [\bar{u}_i(\ell)\Gamma^N v_n(\nu_\ell)] [\bar{u}_m(\nu_\tau)\Gamma_N u_j(\tau)], \quad (1)$$

where G_F is the Fermi constant, i and j are the chirality indices for the charged leptons, n and m are the chirality indices of the neutrinos, ℓ is e or μ , $\Gamma^S = 1$, $\Gamma^V = \gamma^\mu$, $\Gamma^T = i(\gamma^\mu\gamma^\nu - \gamma^\nu\gamma^\mu)/2\sqrt{2}$ are, respectively, the scalar, vector, and tensor Lorentz structures in terms of the Dirac matrices γ^μ , u_i and v_i are the four-component spinors of a particle and an antiparticle, respectively, and g_{ij}^N are the corresponding dimensionless couplings. In the SM, τ^- decays into ν_τ and a W^- -boson, the latter

¹ Unless otherwise stated, use of charge-conjugate modes is implied throughout the paper.

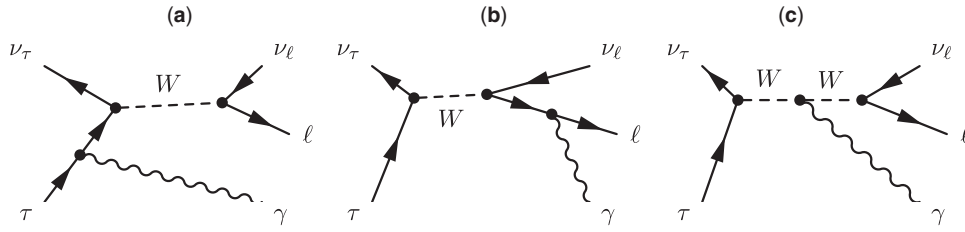


Fig. 1. Three Feynman diagrams of the τ radiative leptonic decay.

decays into ℓ^- and right-handed $\bar{\nu}_\ell$; i.e., the only non-zero coupling is $g_{LL}^V = 1$. Experimentally, only the squared matrix element is observable, and bilinear combinations of the g_{ij}^N are accessible. Of all such combinations, four Michel parameters, η , ρ , δ , and ξ , can be measured in the leptonic decay of the τ when the final-state neutrinos are not observed and the spin of the outgoing lepton is not measured [4]:

$$\rho = \frac{3}{4} - \frac{3}{4} \left(|g_{LR}^V|^2 + |g_{RL}^V|^2 + 2|g_{LR}^T|^2 + 2|g_{RL}^T|^2 + \Re(g_{LR}^S g_{LR}^{T*} + g_{RL}^S g_{RL}^{T*}) \right), \quad (2)$$

$$\eta = \frac{1}{2} \Re(6g_{RL}^V g_{LR}^{T*} + 6g_{LR}^V g_{RL}^{T*} + g_{RR}^S g_{LL}^{V*} + g_{RL}^S g_{LR}^{V*} + g_{LR}^S g_{RL}^{V*} + g_{LL}^S g_{RR}^{V*}), \quad (3)$$

$$\xi = 4\Re(g_{LR}^S g_{LR}^{T*} - g_{RL}^S g_{RL}^{T*}) + |g_{LL}^V|^2 + 3|g_{LR}^V|^2 - 3|g_{RL}^V|^2 - |g_{RR}^V|^2 + 5|g_{LR}^T|^2 - 5|g_{RL}^T|^2 + \frac{1}{4} \left(|g_{LL}^S|^2 - |g_{LR}^S|^2 + |g_{RL}^S|^2 - |g_{RR}^S|^2 \right), \quad (4)$$

$$\xi\delta = \frac{3}{16} \left(|g_{LL}^S|^2 - |g_{LR}^S|^2 + |g_{RL}^S|^2 - |g_{RR}^S|^2 \right) - \frac{3}{4} \left(|g_{LR}^T|^2 - |g_{RL}^T|^2 - |g_{LL}^V|^2 + |g_{RR}^V|^2 - \Re(g_{LR}^S g_{LR}^{T*} + g_{RL}^S g_{RL}^{T*}) \right). \quad (5)$$

The Feynman diagrams describing the radiative leptonic decay of the τ are presented in Fig. 1. The last amplitude, Fig. 1(c), is ignored because this contribution turns out to be suppressed by the very small factor $(m_\tau/m_W)^2$ [5]. As shown in Refs. [6,7], through the presence of a radiative photon in the final state, the polarization of the outgoing lepton is indirectly exposed; accordingly, three more Michel parameters, $\bar{\eta}$, η'' , and $\xi\kappa$, become experimentally accessible:

$$\bar{\eta} = |g_{RL}^V|^2 + |g_{LR}^V|^2 + \frac{1}{8} \left(|g_{RL}^S + 2g_{RL}^T|^2 + |g_{LR}^S + 2g_{LR}^T|^2 \right) + 2 \left(|g_{RL}^T|^2 + |g_{LR}^T|^2 \right), \quad (6)$$

$$\eta'' = \Re \left\{ 24g_{RL}^V (g_{LR}^{S*} + 6g_{LR}^{T*}) + 24g_{LR}^V (g_{RL}^{S*} + 6g_{RL}^{T*}) - 8(g_{RR}^V g_{LL}^{S*} + g_{LL}^V g_{RR}^{S*}) \right\}, \quad (7)$$

$$\xi\kappa = |g_{RL}^V|^2 - |g_{LR}^V|^2 + \frac{1}{8} \left(|g_{RL}^S + 2g_{RL}^T|^2 - |g_{LR}^S + 2g_{LR}^T|^2 \right) + 2 \left(|g_{RL}^T|^2 - |g_{LR}^T|^2 \right). \quad (8)$$

Both $\bar{\eta}$ and η'' appear in spin-independent terms in the differential decay width. Since all terms in Eq. (6) are strictly non-negative, the upper limit on $\bar{\eta}$ provides a constraint on each coupling constant. The effect of the non-zero value of η'' is suppressed by a factor $m_\nu^2/m_\tau^2 \sim 10^{-7}$ for an electron mode and about 4×10^{-3} for a muon mode, and so proves to be difficult to measure with the available statistics collected at Belle. In this study, we fix η'' at its SM value ($\eta'' = 0$).

To measure $\xi\kappa$, which appears in the spin-dependent part of the differential decay width, knowledge of the τ spin direction is required. Although the average polarization of a single τ is zero in

Table 1. Michel parameters of the τ lepton.*

Name	SM value	Spin correlation	Experimental result [11]	Comments
η	0	no	0.013 ± 0.020	ALEPH: [12]
ρ	3/4	no	0.745 ± 0.008	CLEO: [13]
$\xi\delta$	3/4	yes	0.746 ± 0.021	CLEO: [13]
ξ	1	yes	1.007 ± 0.040	Measured in leptonic decays (CLEO: [13])
ξ_h	1	yes	0.995 ± 0.007	Measured in hadronic decays (CLEO: [13])
$\bar{\eta}$	0	no	not measured	From radiative decay (RD)
$\xi\kappa$	0	yes	not measured	From RD
η''	0	no	not measured	From RD, suppressed by m_l^2/m_τ^2
ξ'	1	yes	—	$\xi' = -\xi - 4\xi\kappa + 8\xi\delta/3$
ξ''	1	no	—	$\xi'' = 16\rho/3 - 4\bar{\eta} - 3$

* Experimental results represent average values obtained by PDG [11].

experiments at e^+e^- colliders with unpolarized beams, the spin–spin correlation between the τ^+ and τ^- in the reaction $e^+e^- \rightarrow \tau^+\tau^-$ can be exploited to measure $\xi\kappa$ [8].

According to Ref. [9], $\xi\kappa$ is related to another Michel-like parameter $\xi' = -\xi - 4\xi\kappa + 8\xi\delta/3$. Because the normalized probability that the τ^- decays into the right-handed charged daughter lepton Q_R^τ is given by $Q_R^\tau = (1 - \xi')/2$ [10], measurement of $\xi\kappa$ provides a further constraint on the Lorentz structure of the weak current. The information on these parameters is summarized in Table 1.

In muon decay, through the direct measurement of electron polarization in $\mu^+ \rightarrow e^+\nu_e\bar{\nu}_\mu$, the relevant parameters ξ' and $\xi'' = 16\rho/3 - 4\bar{\eta} - 3$ have already been measured. Those of the τ have not yet been measured.

Using the statistically abundant data set of ordinary leptonic decays, previous measurements [12,13] have determined the Michel parameters η , ρ , δ , and ξ to an accuracy of a few percent and show agreement with the SM prediction. Taking into account this measured agreement, the smaller data set of the radiative decay, and its limited sensitivity, we focus in this analysis only on the extraction of $\bar{\eta}$ and $\xi\kappa$ by fixing η , ρ , δ , ξ , and ξ_ρ to the SM, where ξ_ρ is equal to the negative helicity of ν_τ in the hadronic decay $\tau^- \rightarrow \rho^-\nu_\tau$, and $\xi_\rho = 1$ in the SM. This represents the first measurement of the $\bar{\eta}$ and $\xi\kappa$ parameters of the τ lepton.

2. Method

2.1. Unbinned maximum likelihood method

The differential decay width for the radiative leptonic decay of τ^- with a definite spin direction \mathbf{S}_-^* is given by [7]

$$\frac{d\Gamma(\tau^- \rightarrow \ell^- \nu_\tau \bar{\nu}_\ell \gamma)}{dE_\ell^* d\Omega_\ell^* dE_\gamma^* d\Omega_\gamma^*} = (A_0^- + \bar{\eta} A_1^-) + (\mathbf{B}_0^- + \xi\kappa \mathbf{B}_1^-) \cdot \mathbf{S}_-^*, \quad (9)$$

where A_i^- and \mathbf{B}_i^- ($i = 0, 1$) are known functions of the kinematics of the decay products with indices $i = 0, 1$ (i is the function identifier), Ω_a stands for a set of $\{\cos\theta_a, \phi_a\}$ for a particle of type a , and the asterisk means that the variable is defined in the τ^- rest frame. Equation (9) shows that $\xi\kappa$ appears in the *spin-dependent* part of the decay width. This parameter can be measured by utilizing

the well-known spin–spin correlation of the τ leptons in the $e^-e^+ \rightarrow \tau^+\tau^-$ production:

$$\frac{d\sigma(e^-e^+ \rightarrow \tau^-(\mathbf{S}_-^*)\tau^+(\mathbf{S}_+^*))}{d\Omega_\tau} = \frac{\alpha^2\beta_\tau}{64E_\tau^2}(D_0 + \sum_{i,j} D_{ij}(\mathbf{S}_-^*)_i(\mathbf{S}_+^*)_j), \quad (10)$$

where α is the fine structure constant, β_τ and E_τ are the velocity and energy of the τ^- in the center-of-mass system (c.m.s.), respectively, D_0 is the spin-independent part of the cross section, and D_{ij} ($i, j = 0, 1, 2$) is a tensor describing the spin–spin correlation (see Eq. (4.11) in Ref. [8]). For the partner τ^+ , its spin information is extracted using the two-body decay $\tau^+ \rightarrow \rho^+\bar{\nu}_\tau \rightarrow \pi^+\pi^0\bar{\nu}_\tau$, whose differential decay width is

$$\frac{d\Gamma(\tau^+ \rightarrow \pi^+\pi^0\bar{\nu}_\tau)}{d\Omega_\rho^* dm^2 d\tilde{\Omega}_\pi} = A^+ + \xi_\rho \mathbf{B}^+ \cdot \mathbf{S}_+^*; \quad (11)$$

A^+ and \mathbf{B}^+ are known functions for the spin-independent and spin-dependent parts, respectively; the tilde indicates variables defined in the ρ^+ rest frame, and m is the invariant mass of the $\pi\pi^0$ system, $m^2 = (p_\pi + p_{\pi^0})^2$. As mentioned before, we use the SM value: $\xi_\rho = 1$. Thus, the total differential cross section of $e^+e^- \rightarrow \tau^-\tau^+ \rightarrow (\ell^-\nu_\tau\bar{\nu}_\ell\gamma)(\pi^+\pi^0\bar{\nu}_\tau)$ [or, briefly, $(\ell^-\gamma, \pi^+\pi^0)$] can be written as:

$$\frac{d\sigma(\ell^-\gamma, \pi^+\pi^0)}{dE_\ell^* d\Omega_\ell^* dE_\gamma^* d\Omega_\gamma^* d\Omega_\rho^* dm^2 d\tilde{\Omega}_\pi d\Omega_\tau} \propto \frac{\beta_\tau}{E_\tau^2} \left[D_0 (A_0^- + A_1^- \cdot \bar{\eta}) A^+ + \sum_{i,j} D_{ij}(\mathbf{B}_0^- + \mathbf{B}_1^- \cdot \xi\kappa)_i (\mathbf{B}^+)_j \right]. \quad (12)$$

To extract the visible differential cross section, we transform the differential variables into ones defined in the c.m.s.² using the Jacobian J :

$$J = \left| \frac{\partial(E_\ell^*, \Omega_\ell^*)}{\partial(P_\ell, \Omega_\ell)} \right| \left| \frac{\partial(E_\gamma^*, \Omega_\gamma^*)}{\partial(P_\gamma, \Omega_\gamma)} \right| \left| \frac{\partial(\Omega_\rho^*, \Omega_\tau)}{\partial(P_\rho, \Omega_\rho, \Phi)} \right| = \left(\frac{P_\ell^2}{E_\ell P_\ell^*} \right) \left(\frac{E_\gamma}{E_\gamma^*} \right) \left(\frac{m_\tau P_\rho}{E_\rho P_\rho^* P_\tau} \right), \quad (13)$$

where the parameter Φ denotes the angle along the arc illustrated in Fig. 2.

The visible differential cross section is, therefore, obtained by integration over Φ :

$$\frac{d\sigma(\ell^-\gamma, \pi^+\pi^0)}{dP_\ell d\Omega_\ell dP_\gamma d\Omega_\gamma dP_\rho d\Omega_\rho dm^2 d\tilde{\Omega}_\pi} = \int_{\Phi_1}^{\Phi_2} d\Phi \frac{d\sigma(\ell^-\gamma, \pi^+\pi^0)}{d\Phi dP_\ell d\Omega_\ell dP_\gamma d\Omega_\gamma dP_\rho d\Omega_\rho dm^2 d\tilde{\Omega}_\pi} \quad (14)$$

$$= \int_{\Phi_1}^{\Phi_2} d\Phi \frac{d\sigma(\ell^-\gamma, \pi^+\pi^0)}{dE_\ell^* d\Omega_\ell^* dE_\gamma^* d\Omega_\gamma^* d\Omega_\rho^* dm^2 d\tilde{\Omega}_\pi d\Omega_\tau} J \quad (15)$$

$$\equiv S(\mathbf{x}), \quad (16)$$

where $S(\mathbf{x})$ is proportional to the probability density function (PDF) of the signal, and \mathbf{x} denotes the set of 12 measured variables: $\mathbf{x} = \{P_\ell, \Omega_\ell, P_\gamma, \Omega_\gamma, P_\rho, \Omega_\rho, m^2, \tilde{\Omega}_\pi\}$. There are several corrections that must be incorporated in the procedure to take into account the real experimental situation. Physics corrections include electroweak higher-order corrections to the $e^+e^- \rightarrow \tau^+\tau^-$ cross section [14–18]. Apparatus corrections include the effect of the finite detection efficiency and resolution, the effect of the external bremsstrahlung for $(e^-\gamma, \pi^+\pi^0)$ events, and the e^\pm beam energy spread.

² Throughout in this paper, c.m.s. stands for the center of mass system of electron and positron beams unless otherwise stated.

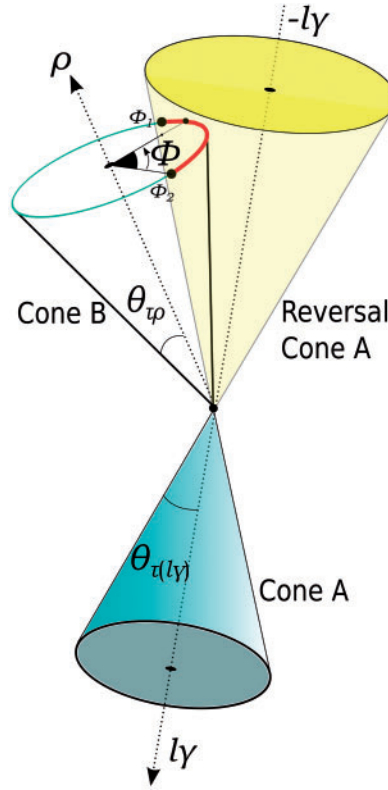


Fig. 2. Kinematics of $\tau^+\tau^- \rightarrow (\rho^+ (\rightarrow \pi^+\pi^0)\bar{\nu}_\tau)(\ell^- \nu_\tau \bar{\nu}_\ell \gamma)$ decay. Cones A and B are the surfaces that satisfy the c.m.s. conditions $(p_{\tau^-} - p_{\ell-\gamma})^2 = 0$ and $(p_{\tau^+} - p_{\rho^+})^2 = 0$, respectively. The direction of τ^+ momentum (defined from the e^+e^- interaction point) lies on an arc defined by the intersection of cone B and the interior sector constrained by the reversal (i.e., mirror) cone A. The arc (shown in red) is parametrized by the angle $\Phi \in [\Phi_1, \Phi_2]$.

Accounting for the event-selection criteria and the contamination from identified backgrounds, the total visible (properly normalized) PDF for the observable \mathbf{x} in each event is given by

$$P(\mathbf{x}) = \left(1 - \sum_i \lambda_i\right) \frac{S(\mathbf{x})\varepsilon(\mathbf{x})}{\int d\mathbf{x}S(\mathbf{x})\varepsilon(\mathbf{x})} + \sum_i \lambda_i \frac{B_i(\mathbf{x})\varepsilon(\mathbf{x})}{\int d\mathbf{x}B_i(\mathbf{x})\varepsilon(\mathbf{x})}, \quad (17)$$

where $B_i(\mathbf{x})$ is the distribution of the i th category of background, λ_i is the fraction of this background, and $\varepsilon(\mathbf{x})$ is the selection efficiency of the signal distribution. The categorization of i is explained later (see the caption of Fig. 3). In general, the selection efficiencies differ between signal and backgrounds; however, the relative difference of background efficiency is included in the definition of $B_i(\mathbf{x})$. $B_i(\mathbf{x})$ is evaluated as an integral of the i th background PDF multiplied by the inefficiency that depends on the variables of missing particles. For example, if $\tau^+ \rightarrow \pi^+\pi^0\pi^0\bar{\nu}_\tau$ is misreconstructed as $\tau^+ \rightarrow \pi^+\pi^0\bar{\nu}_\tau$, the PDF of the $(\tau^+ \rightarrow \pi^+\pi^0\pi^0\nu_\tau)(\tau^- \rightarrow \ell^-\nu_\tau\nu_\ell\gamma)$ process is multiplied by the π^0 reconstruction inefficiency and integrated over the allowed π^0 phase space. The PDFs of the dominant background processes are described analytically one by one, while the remaining background processes are described by one common PDF, tabulated from Monte Carlo (MC) simulation.

The denominator of the signal term in Eq. (17) represents normalization. Since $S(\mathbf{x})$ is a linear combination of the Michel parameters, $S(\mathbf{x}) = \mathcal{S}_0(\mathbf{x}) + \mathcal{S}_1(\mathbf{x})\bar{\eta} + \mathcal{S}_2(\mathbf{x})\xi\kappa$, the normalization of the

signal PDF becomes:

$$\begin{aligned}
& \int d\mathbf{x} \left(\mathcal{S}_0(\mathbf{x}) + \mathcal{S}_1(\mathbf{x})\bar{\eta} + \mathcal{S}_2(\mathbf{x})\xi\kappa \right) \varepsilon(\mathbf{x}) \\
&= \mathcal{N}_0 \int d\mathbf{x} \left(\frac{\mathcal{S}_0(\mathbf{x})\varepsilon(\mathbf{x})}{\mathcal{N}_0} \right) \cdot \frac{\mathcal{S}_0(\mathbf{x}) + \mathcal{S}_1(\mathbf{x})\bar{\eta} + \mathcal{S}_2(\mathbf{x})\xi\kappa}{\mathcal{S}_0(\mathbf{x})} \\
&= \frac{\mathcal{N}_0\bar{\varepsilon}}{N_{\text{sel}}} \sum_{i:\text{sel}} \frac{\mathcal{S}_0(\mathbf{x}^i) + \mathcal{S}_1(\mathbf{x}^i)\bar{\eta} + \mathcal{S}_2(\mathbf{x}^i)\xi\kappa}{\mathcal{S}_0(\mathbf{x}^i)} \\
&= \mathcal{N}_0\bar{\varepsilon} \left[1 + \left\langle \frac{\mathcal{S}_1}{\mathcal{S}_0} \right\rangle \bar{\eta} + \left\langle \frac{\mathcal{S}_2}{\mathcal{S}_0} \right\rangle \xi\kappa \right], \tag{18}
\end{aligned}$$

where \mathcal{N}_0 is a normalization coefficient of the SM part defined by $\mathcal{N}_0 = \int d\mathbf{x} \mathcal{S}_0(\mathbf{x})$, \mathbf{x}^i represents a set of variables for the i th selected event of N_{sel} events, $\bar{\varepsilon}$ is an average selection efficiency, and the brackets $\langle \rangle$ indicate an average with respect to the selected SM distribution. We refer to \mathcal{N}_0 and $\langle \mathcal{S}_i/\mathcal{S}_0 \rangle$ ($i = 1, 2$) as absolute and relative normalizations, respectively.

From $P(\mathbf{x})$, the negative logarithmic likelihood function (NLL) is constructed and the best estimators of the Michel parameters, $\bar{\eta}$ and $\xi\kappa$, are obtained by minimizing the NLL. The efficiency $\varepsilon(\mathbf{x})$ is a common multiplier in Eq. (17) and does not depend on the Michel parameters. This is one of the essential features of the unbinned maximum likelihood method. We validated our fitter and procedures using an MC sample generated according to the SM distribution. The best-fit values of the Michel parameters are consistent with their SM expectations within the statistical uncertainties.

2.2. KEKB collider

The KEKB collider (KEK laboratory, Tsukuba, Japan) is an energy-asymmetric e^+e^- collider with beam energies of 3.5 GeV and 8.0 GeV for e^+ and e^- , respectively. Most of the data were taken at the c.m.s. energy of 10.58 GeV, corresponding to the mass of the $\Upsilon(4S)$, where a huge number of $\tau^+\tau^-$ as well as $B\bar{B}$ pairs were produced. The KEKB collider was operated from 1999 to 2010 and accumulated 1 ab^{-1} of e^+e^- collision data with the Belle detector. The achieved instantaneous luminosity of $2.11 \times 10^{34} \text{ cm}^{-2} \text{ s}^{-1}$ is the world record. For this reason, the KEKB collider is often called a B -factory, but it is worth considering it also as a τ -factory, where $O(10^9)$ τ pair events have been produced. The world's largest sample of τ leptons collected at Belle provides a unique opportunity to study radiative leptonic decay of τ . In this analysis, we use 711 fb^{-1} of collision data collected at the $\Upsilon(4S)$ resonance energy (see Ref. [19] and other papers in that volume, and Ref. [20] and references therein).

2.3. Belle detector

The Belle detector is a large-solid-angle magnetic spectrometer that consists of a silicon vertex detector, a 50-layer central drift chamber (CDC), an array of aerogel threshold Cherenkov counters (ACC), a barrel-like arrangement of time-of-flight scintillation counters (TOF), and an electromagnetic calorimeter comprising CsI(Tl) crystals (ECL) located inside a superconducting solenoid coil that provides a 1.5 T magnetic field. An iron flux return located outside of the coil is instrumented to detect K_L^0 mesons and to identify muons (KLM). The detector is described in detail elsewhere [21,22].

3. Event selection

The event selection proceeds in two stages. At the preselection, $\tau^+\tau^-$ candidates are selected efficiently while suppressing the beam background and other physics processes like radiative Bhabha scattering, two-photon interaction, and radiative $\mu^+\mu^-$ pair production. The preselected events are then required to satisfy final selection criteria to enhance the purity of the signal events.

3.1. Preselection

- There must be exactly two oppositely charged tracks in the event. The impact parameters of these tracks relative to the interaction point are required to be within ± 2.5 cm along the beam axis and ± 0.5 cm in the transverse plane. The transverse momentum, P_t , of each track must exceed 0.1 GeV/ c and the track with the largest P_t must satisfy $P_t > 0.5$ GeV/ c .
- Total energy deposition in the ECL in the laboratory frame must be lower than 9 GeV.
- The opening angle ψ of the two tracks must satisfy $20^\circ < \psi < 175^\circ$ in the laboratory frame.
- The number of photons whose energy exceeds 80 MeV in the c.m.s. must be less than five.
- For the four-vector of missing momentum defined by $p_{\text{miss}} = p_{\text{beam}} - p_{\text{obs}}$, the missing mass M_{miss} defined by $M_{\text{miss}}^2 = p_{\text{miss}}^2/c^2$ must lie in the range $1 \text{ GeV}/c^2 \leq M_{\text{miss}} \leq 7 \text{ GeV}/c^2$, where p_{beam} and p_{obs} are the four-momenta of the beam and all detected particles, respectively.
- The polar angle (in the spherical system of coordinates in c.m.s., where the z axis is antiparallel to the positron beam) of the missing momentum, θ_{miss} , must satisfy $30^\circ \leq \theta_{\text{miss}} \leq 150^\circ$.

3.2. Final selection

The candidates for the outgoing particles in $\tau^+\tau^- \rightarrow (\pi^+\pi^0\bar{\nu}_\tau)(\ell^-\nu_\tau\bar{\nu}_\ell\bar{\omega}\gamma)$, i.e., the lepton, photon, and charged and neutral pions, are assigned in each of the preselected events.

- The electron identification is based on the likelihood ratio selection, $P_e = L_e/(L_e + L_x) > 0.9$, where L_e and L_x are the likelihood values of the track for the electron and non-electron hypotheses, respectively. These values are determined using specific ionization (dE/dx) in the CDC, the ratio of ECL energy and CDC momentum E/P , the transverse shape of the cluster in the ECL, the matching of the track with the ECL cluster, and the light yield in the ACC [23]. The muon identification uses the likelihood ratio $P_\mu = L_\mu/(L_\mu + L_\pi + L_K) > 0.9$, where the likelihood values are determined by the measured versus expected range for the μ hypothesis, and transverse scattering of the track in the KLM [24]. The reductions of the signal efficiencies with lepton selections are approximately 10% and 30% for the electron and muon, respectively. The pion candidates are distinguished from kaons using $P_\pi = L_\pi/(L_\pi + L_K) > 0.4$, where the likelihood values are determined by the ACC response, the timing information from the TOF, and dE/dx in the CDC. The reduction of the signal efficiency with pion selection is approximately 5%.
- The π^0 candidate is formed from two photon candidates, where each photon satisfies $E_\gamma > 80$ MeV, with an invariant mass of $115 \text{ MeV}/c^2 < M_{\gamma\gamma} < 150 \text{ MeV}/c^2$. Figure 3 shows the distribution of the invariant mass of the π^0 candidates. The reduction of the signal efficiency by the mass selection is approximately 50%. In addition, when more than one π^0 candidates are found, the event is rejected.
- The ρ^+ candidate is formed from a π^+ and a π^0 candidate, with an invariant mass of $0.5 \text{ GeV}/c^2 < M_{\pi^+\pi^0} < 1.5 \text{ GeV}/c^2$. Figure 4 shows the distribution of the invariant mass of the ρ candidates. The reduction of the signal efficiency is approximately 3%.

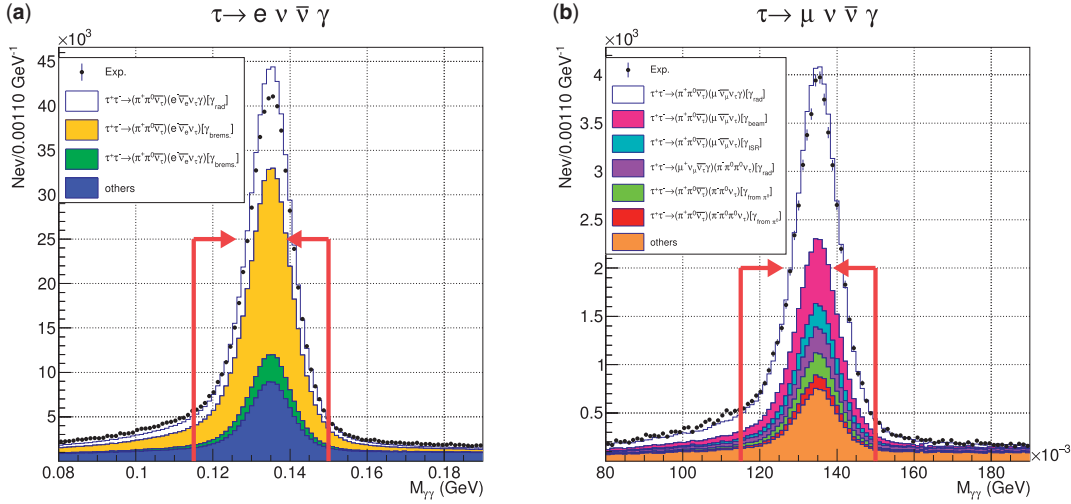


Fig. 3. Distribution of $M_{\gamma\gamma}$. Dots with uncertainties are experimental data and histograms are MC distributions. The MC histograms are scaled to the experimental one based on the yields just after the preselection. The red arrows indicate the selection window $115 \text{ MeV}/c^2 < M_{\gamma\gamma} < 150 \text{ MeV}/c^2$. (a) $\tau^- \rightarrow e^- \nu_\tau \bar{\nu}_e \gamma$ candidates: the open histogram corresponds to the signal, the yellow and green histograms represent ordinary leptonic decay plus external bremsstrahlung on the detector material and radiative leptonic decay plus bremsstrahlung, respectively, and the blue histogram represents other processes such as radiative Bhabha, two-photon, and $e^+ e^- \rightarrow q\bar{q}$ ($q = u, d, s, c$) productions. (b) $\tau^- \rightarrow \mu^- \nu_\tau \bar{\nu}_\mu \gamma$ candidates: the open histogram corresponds to signal, the magenta histogram represents ordinary leptonic decay plus beam background, the aqua histogram represents ordinary leptonic decay plus ISR/FSR processes, the purple histogram represents three-pion events where $\tau^+ \rightarrow \pi^+ \pi^0 \pi^0 \bar{\nu}_\tau$ is misreconstructed as a tagging $\tau^+ \rightarrow \pi^+ \pi^0 \bar{\nu}_\tau$ candidate, the green histogram represents ρ - ρ background where $\tau^- \rightarrow \pi^- \pi^0 \nu_\tau$ is selected due to misidentification of pion as muon, the red histogram represents 3π - ρ events where $\tau^- \rightarrow \pi^- \pi^0 \pi^0 \nu_\tau$ is selected by misidentification similarly to the ρ - ρ case, and the orange histogram represents other processes (as in the electron mode).

- The c.m.s. energy of the signal photon candidate must exceed 80 MeV if within the ECL barrel ($31.4^\circ < \theta_\gamma < 131.5^\circ$) or 100 MeV if within the ECL endcaps ($12.0^\circ < \theta_\gamma < 31.4^\circ$ or $131.5^\circ < \theta_\gamma < 157.1^\circ$). As shown in Fig. 5, this photon must lie in a cone determined by the lepton-candidate direction that is defined by $\cos\theta_{e\gamma} > 0.9848$ and $\cos\theta_{\mu\gamma} > 0.9700$ for the electron and muon mode, respectively, where $\theta_{\ell\gamma}$ ($\ell = e$ or μ) is the angle between the lepton and the photon. The reductions of the signal efficiencies for the requirement on this photon direction are approximately 11% and 27% for the electron and muon mode, respectively. Furthermore, if the photon candidate and either of the photons from the π^0 , which is a daughter of the ρ^+ candidate, form an invariant mass of the π^0 ($115 \text{ MeV}/c^2 < M_{\gamma\gamma} < 150 \text{ MeV}/c^2$), the event is rejected. The additional selection reduces the signal efficiency by 1%.
- The direction of the combined momentum of the lepton and photon in the c.m.s. must not belong to the hemisphere determined by the ρ candidate: an event should satisfy $\theta_{(\ell-\gamma)\rho^+} > 90^\circ$, where $\theta_{(\ell-\gamma)\rho^+}$ is the spatial angle between the $\ell^- \gamma$ system and the ρ candidate. This selection reduces the signal efficiency by 0.4%.
- There must be no additional photons in the aforementioned cone ($\cos\theta_{e\gamma} > 0.9848$ and $\cos\theta_{\mu\gamma} > 0.9700$ for the electron and muon mode, respectively) around the lepton candidate; the sum of the energy in the laboratory frame of all additional photons that are not associated with the π^0 or the signal photon (denoted as $E_{\text{extra}\gamma}^{\text{LAB}}$) should not exceed 0.2 GeV and 0.3 GeV for the electron and muon mode, respectively. The reductions of the signal efficiencies for

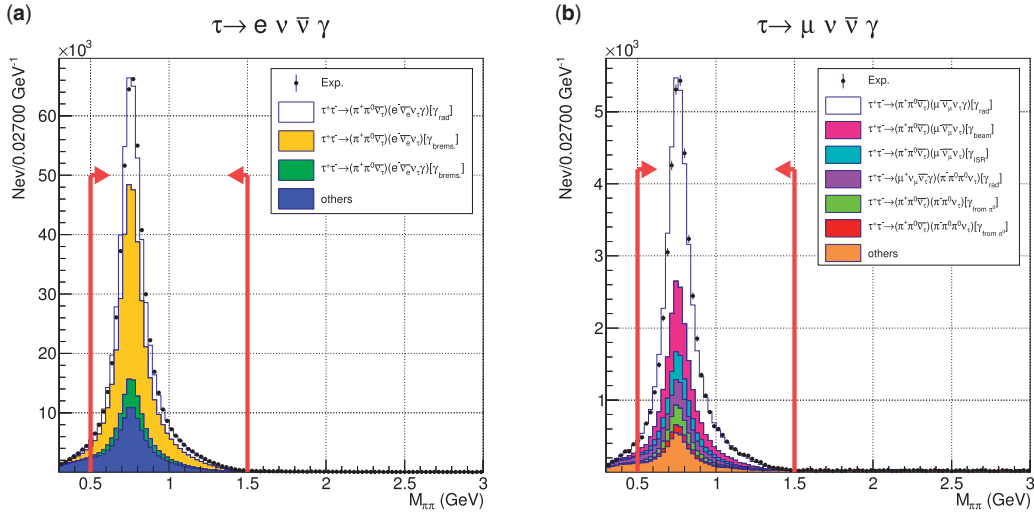


Fig. 4. Distribution of $M_{\pi\pi^0}$: (a) $\tau^- \rightarrow e^- \nu_\tau \bar{\nu}_e \gamma$ candidates and (b) $\tau^- \rightarrow \mu^- \nu_\tau \bar{\nu}_\mu \gamma$ candidates. Dots with uncertainties are experimental data and histograms are MC distributions. The color of each histogram is explained in Fig. 3. The red arrows indicate the selection window $0.5 \text{ GeV}/c^2 < M_{\pi\pi^0} < 1.5 \text{ GeV}/c^2$.

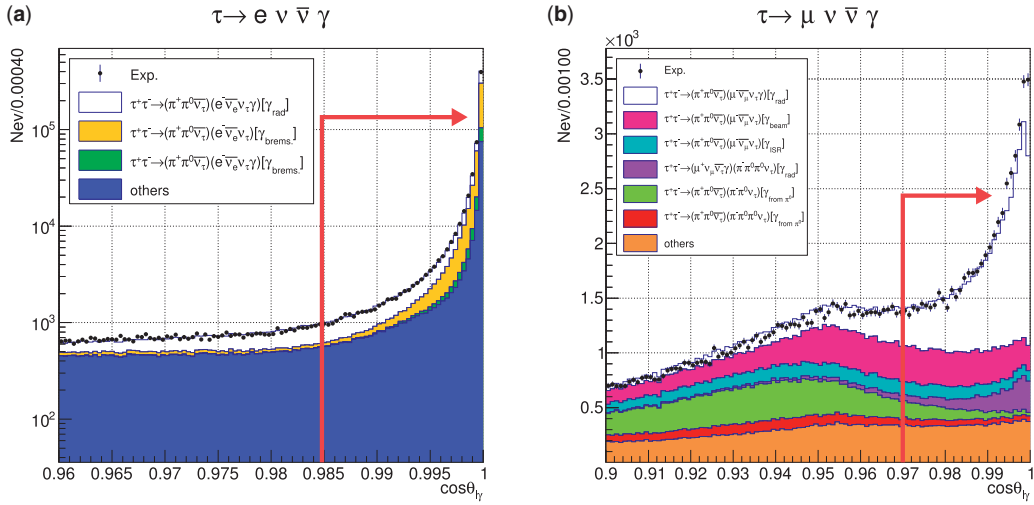


Fig. 5. Distribution of $\cos\theta_{\ell\gamma}$: (a) $\tau^- \rightarrow e^- \nu_\tau \bar{\nu}_e \gamma$ candidates and (b) $\tau^- \rightarrow \mu^- \nu_\tau \bar{\nu}_\mu \gamma$ candidates. Dots with uncertainties are experimental data and histograms are MC distributions. The color of each histogram is explained in Fig. 3. The red arrows indicate the selection condition $\cos\theta_{e\gamma} > 0.9848$ and $\cos\theta_{\mu\gamma} > 0.9700$ for the electron and muon mode, respectively.

the requirement on $E_{\text{extra}}^{\text{LAB}}$ are approximately 14% and 6% for the electron and muon mode, respectively.

- In this analysis we use two types of triggers, the neutral trigger (N) and the charged trigger (Z), which provide sufficient redundancy. The neutral trigger is based on the information from the ECL. In particular, we select events whose ECL response pattern differs from that of the cosmic muons (the so-called ECL cosmic veto), and there are at least four isolated clusters with energy thresholds of 0.11 GeV [25]. The charged trigger is based on information from the CDC and KLM [26]. Neither trigger uses the so-called Bhabha veto, which is why their efficiencies, ε_N and

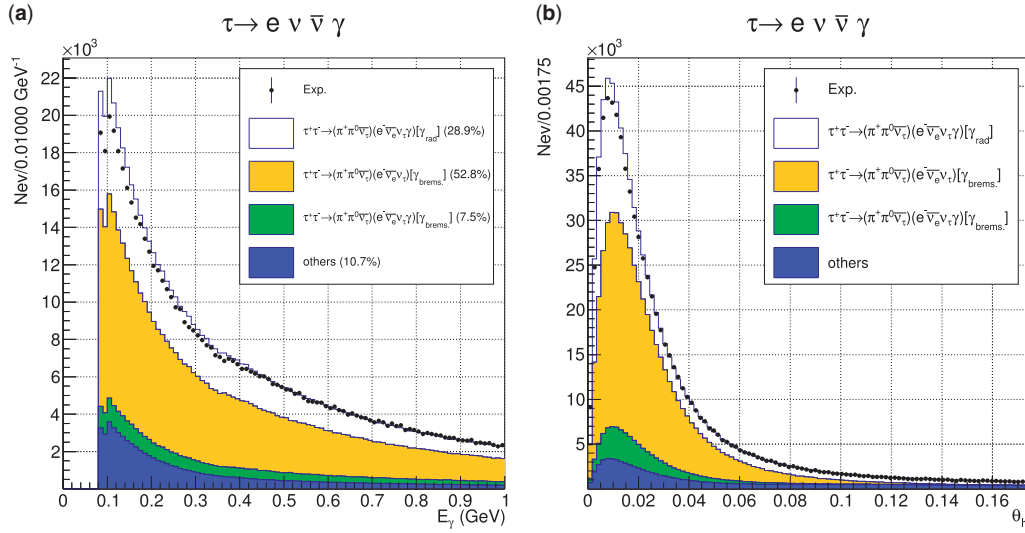


Fig. 6. Final distribution of (a) photon energy E_γ and (b) $\theta_{e\gamma}$ for the $\tau^+\tau^- \rightarrow (\pi^+\pi^0\nu_\tau)(e^-\nu_\tau\bar{\nu}_e\gamma)$ decay candidates. Dots with uncertainties are experimental data, and histograms are MC distributions. The color of each histogram is explained in Fig. 3.

ε_Z , are uniform functions on the various kinematical parameters in the selected two-track events. Once N and Z are based on signals from physically independent subsystems, the efficiency of each trigger can be evaluated as: $\varepsilon_N = N_{N\&Z}/N_Z$, $\varepsilon_Z = N_{N\&Z}/N_N$, where $N_{N\&Z}$ is the number of the events triggered by N and Z , and $N_N(N_Z)$ is the number of events triggered by $N(Z)$. Once we select events triggered by N or Z , the trigger efficiency, $\varepsilon_{\text{trg}} = 1 - (1 - \varepsilon_N)(1 - \varepsilon_Z)$, can be evaluated independently for the experimental ($\varepsilon_{\text{trg}}^{\text{EXP}}$) and MC ($\varepsilon_{\text{trg}}^{\text{MC}}$) data samples.

These selection criteria are optimized using MC simulation (five times as large as real data) where $e^+e^- \rightarrow \tau^+\tau^-$ pair production and the successive decay of the τ are simulated by the KKMC [27] and TAUOLA [28,29] generators, respectively. The detector effects are simulated based on the GEANT3 package [30].

Distributions of the photon energy E_γ and the angle between the lepton and photon, $\theta_{\ell\gamma}$, for the selected events are shown in Figs. 6 and 7 for $\tau^- \rightarrow e^-\nu_\tau\bar{\nu}_e\gamma$ and $\tau^- \rightarrow \mu^-\nu_\tau\bar{\nu}_\mu\gamma$ candidates, respectively.

In the electron mode, the fraction of the signal decay in the selected sample is about 30% due to the large external bremsstrahlung rate in the non-radiative leptonic τ decay events. In the muon mode, the fraction of the signal decay is about 60%; here, the main background arises from ordinary leptonic decay ($\tau^- \rightarrow \ell^-\nu_\tau\bar{\nu}_\ell$) events where either an additional photon is reconstructed from the beam background in the ECL or a photon is emitted by the initial-state e^+e^- . The information is summarized in Table 2.

As mentioned before, in the integration over Φ in Eq. (15), the generated differential variables are varied according to the resolution function \mathcal{R} . Thus, the kinematic variables can extend outside the allowed phase space. For the unphysical values, we assign zero to the integrand because this implies negative neutrino masses. If such discarded trials in the integration exceed 20% of the total number of iterations, we reject the event. This happens for events that lie near the kinematical boundary of the signal phase space. The corresponding reduction of the efficiency is approximately 2% and

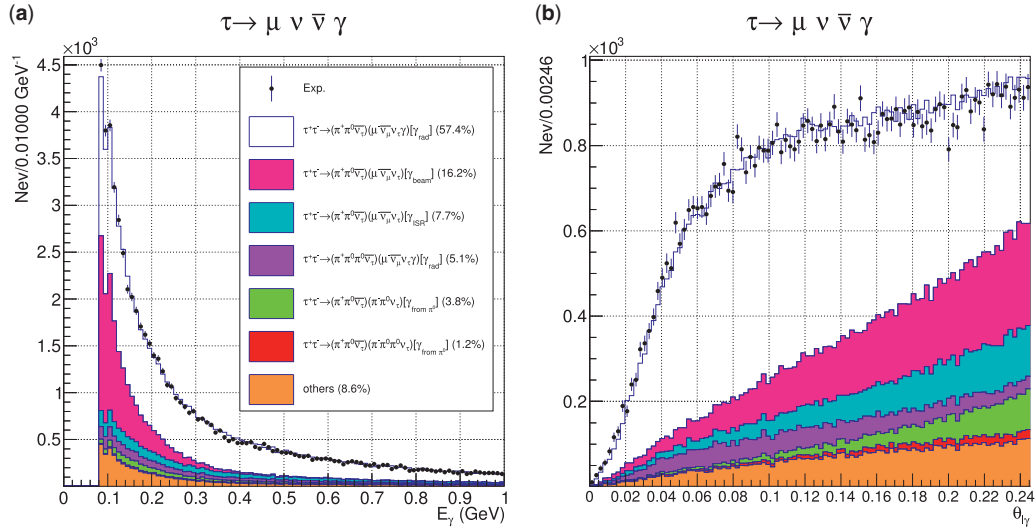


Fig. 7. Final distribution of (a) photon energy E_γ and (b) $\theta_{\mu\gamma}$ for the $\tau^+\tau^- \rightarrow (\pi^+\pi^0\nu_\tau)(\mu^-\nu_\tau\bar{\nu}_\mu\gamma)$ decay candidates. Dots with uncertainties are experimental data, and histograms are MC distributions. The color of each histogram is explained in Fig. 3.

Table 2. Summary of event selection.

Item	$(e^-\nu_\tau\bar{\nu}_e\gamma)(\pi^+\pi^0\bar{\nu}_\tau)$	$(e^+\nu_e\bar{\nu}_\tau\gamma)(\pi^-\pi^0\nu_\tau)$	$(\mu^-\nu_\tau\bar{\nu}_\mu\gamma)(\pi^+\pi^0\bar{\nu}_\tau)$	$(\mu^+\nu_\mu\bar{\nu}_\tau\gamma)(\pi^-\pi^0\nu_\tau)$
N_{sel}	391954	384880	35198	35973
$\bar{\varepsilon}^*$ (%)	4.28 ± 0.24	4.25 ± 0.23	3.58 ± 0.19	3.56 ± 0.18
Purity (%)		28.9 ± 0.8		57.4 ± 1.3

The efficiency is determined based on the photon energy threshold of $E_\gamma^ > 10$ MeV in the τ rest frame. The uncertainties of purity and efficiency include both statistical and systematic effects.

3% for the electron and muon mode, respectively. This additional decrease of the efficiency is not reflected in the values of Table 2.

4. Analysis of experimental data

When we fit the Michel parameters for the real experimental data, the difference in selection efficiency between real data and MC simulation must be taken into account by the correction factor $R(\mathbf{x}) = \varepsilon^{\text{EX}}(\mathbf{x})/\varepsilon^{\text{MC}}(\mathbf{x})$, which is close to unity; its extraction is described below. With this correction, Eq. (17) is modified to

$$P^{\text{EX}}(\mathbf{x}) = \left(1 - \sum_i \lambda_i\right) \cdot \frac{S(\mathbf{x})\varepsilon^{\text{MC}}(\mathbf{x})R(\mathbf{x})}{\int d\mathbf{x}S(\mathbf{x})\varepsilon^{\text{MC}}(\mathbf{x})R(\mathbf{x})} + \sum_i \lambda_i \frac{B_i(\mathbf{x})\varepsilon^{\text{MC}}(\mathbf{x})R(\mathbf{x})}{\int d\mathbf{x}B_i(\mathbf{x})\varepsilon^{\text{MC}}(\mathbf{x})R(\mathbf{x})}. \quad (19)$$

The presence of $R(\mathbf{x})$ in the numerator does not affect the NLL minimization, but its presence in the denominator does.

We evaluate $R(\mathbf{x})$ as the product of the measured corrections for the trigger, particle identification, track, π^0 , and γ reconstruction efficiencies:

$$R(\mathbf{x}) = R_{\text{trg}}R_\ell(P_\ell, \cos\theta_\ell)R_\gamma(P_\gamma, \cos\theta_\gamma)R_\pi(P_\pi, \cos\theta_\pi)R_{\pi^0}(P_{\pi^0}, \cos\theta_{\pi^0}), \quad (20)$$

$$R_\ell(P_\ell, \cos\theta_\ell) = R_{\text{trk}}(P_\ell, \cos\theta_\ell)R_{\text{LID}}(P_\ell, \cos\theta_\ell), \quad (21)$$

$$R_\pi(P_\pi, \cos\theta_\pi) = R_{\text{trk}}(P_\pi, \cos\theta_\pi)R_{\text{PID}}(P_\pi, \cos\theta_\pi). \quad (22)$$

The lepton identification efficiency correction is estimated using two-photon processes $e^+e^- \rightarrow e^+e^-\ell^+\ell^-$ ($\ell = e$ or μ). Since the momentum of the lepton from the two-photon process ranges from the detector threshold to approximately 4 GeV/ c in the laboratory frame, the efficiency correction factor can be evaluated for our signal process as a function of P_ℓ and $\cos\theta_\ell$. The average efficiency correction from lepton identification was found to be 2% and 1% for electron and muon modes, respectively.

The charged pion identification (π ID) correction factor is obtained by the measurement of $D^{*+} \rightarrow D^0\pi_s^+ \rightarrow (K^-\pi^+)\pi_s^+$ decay (where the subscript s indicates ‘‘slow’’). The small momentum of the pion from D^{*+} allows us to select this process. As a result, assuming the mass of the D^0 meson, we can reconstruct D^{*+} even if this π^+ is missed. The average efficiency correction from π ID was found to be 0.7%.

The track reconstruction efficiency correction is extracted from $\tau^+\tau^- \rightarrow (\ell^+\nu_\ell\bar{\nu}_\tau)(\pi^-\pi^+\pi^-\nu_\tau)$ events. Here, we count the number of events N_4 (N_3) in which four (three) charged tracks are reconstructed. The three-track event is required to have a negative net charge (π^+ is missing). Since the charged track reconstruction efficiency ε is included as, respectively, ε^4 and $\varepsilon^3(1-\varepsilon)$ in N_4 and N_3 , the value of ε can be obtained by $\varepsilon = N_4/(N_4 + N_3)$. The momentum and angular dependences of ε are extracted by modifying $N_4 \rightarrow \Delta N_4$, where ΔN_4 is the number of observed events in a certain cell of the phase space of the reconstructed track. The average efficiency correction from tracking was found to be 2%.

The π^0 reconstruction efficiency correction is obtained by comparing the ratio of the number of selected events of $\tau^+\tau^- \rightarrow (\pi^+\pi^0\bar{\nu}_\tau)(\pi^-\pi^0\nu_\tau)$ and $\tau^+\tau^- \rightarrow (\pi^+\pi^0\bar{\nu}_\tau)(\pi^-\nu_\tau)$ between experiment and MC simulation. The momentum and angular dependence of the π^0 reconstruction efficiency is extracted by counting the number of events observed in a certain kinematic-variable cell of the π^0 phase space. By randomly choosing either of the photon daughters from the π^0 , the γ reconstruction efficiency correction is extracted in the same manner. The average efficiency correction for the π^0 reconstruction was found to be 4%.

The trigger efficiency correction $R_{\text{trg}} = \varepsilon_{\text{trg}}^{\text{EXP}}/\varepsilon_{\text{trg}}^{\text{MC}}$ has the largest impact among these factors, although the deviation of the average trigger efficiency correction from unity is only about 1%.

Figure 8 shows the distribution of the momentum and the cosine of the polar angle of electron and muon events. In the figure, the effects of all the corrections are seen mainly at $\cos\theta_e < -0.6$ and $\cos\theta_\mu < -0.6$.

5. Evaluation of systematic uncertainties

In Table 3 we summarize the contributions of the identified sources of systematic uncertainties. The detailed contributions to the efficiency corrections, explained in the previous section, are separately summarized in Table 4.

The dominant source for the electron mode is the calculation of the relative normalizations. Due to the peculiarity of the signal PDF when $m_\ell \rightarrow m_e$, the convergence of the relative normalization coefficients is quite slow and results in a notable effect. For a given number of MC events N , the errors of the relative normalizations $\langle \mathcal{S}_i/\mathcal{S}_0 \rangle$ ($i = 1, 2$) are evaluated by $\sigma^2 = \text{Var}(\mathcal{S}_i/\mathcal{S}_0)/N$, where $\text{Var}(X)$ represents the variance of a random variable X . The resulting systematic effect on the Michel parameter is estimated by varying the normalizations using MC simulation. The effect of the absolute normalization is estimated in the same way.

The largest systematic uncertainty for the muon mode is due to the limited precision of the description of the background PDF that appears in Eq. (19). As mentioned before, the remaining background

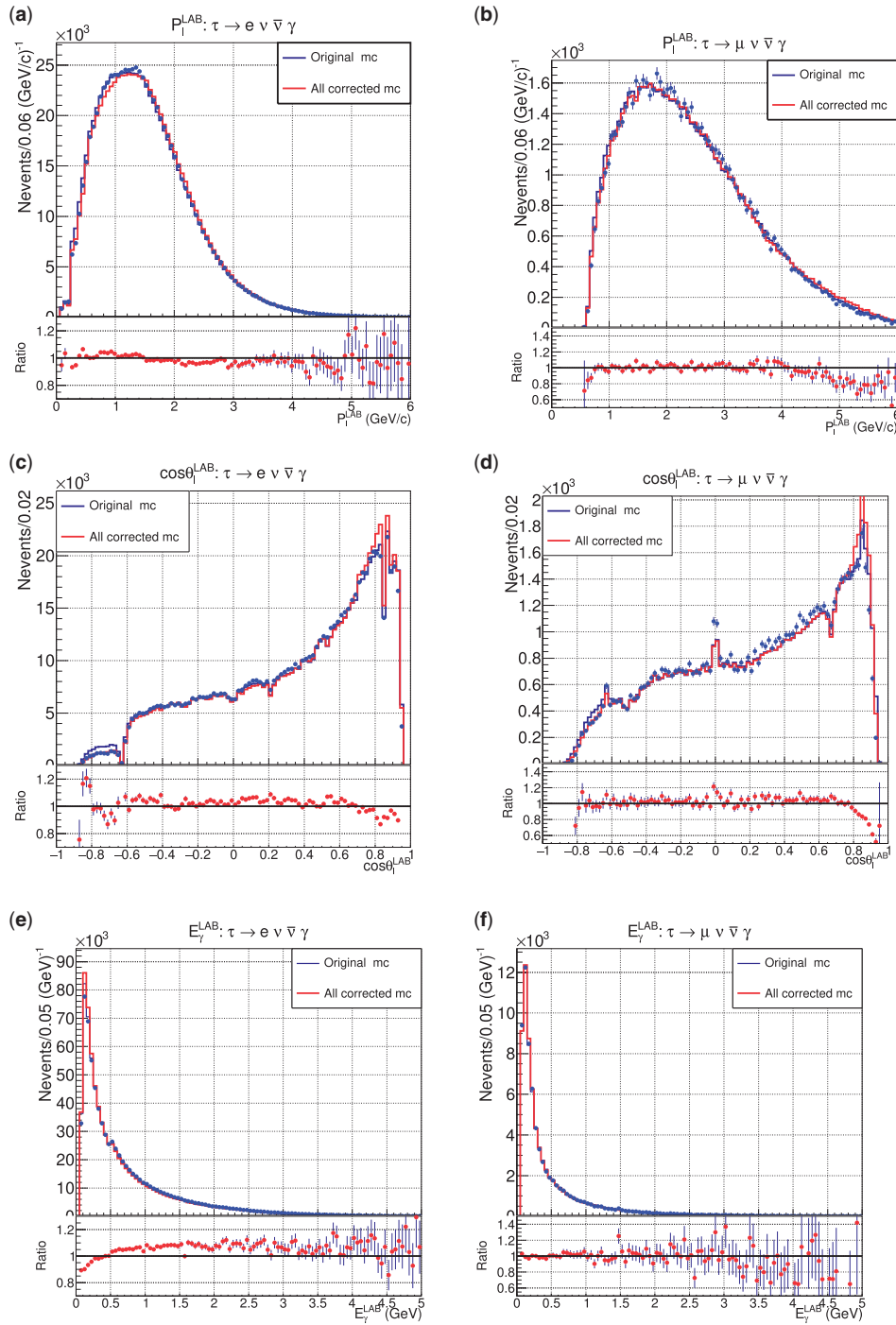


Fig. 8. Distributions of momenta of leptons, cosine of angles and photon energy: (a), (c), (e) for the electron modes, and (b), (d), (f) for the muon modes. The blue points with uncertainties represent the experimental data, while the black and red lines represent the distributions of the original and corrected MC simulation, respectively.

sources are described by a common PDF, which is tabulated utilizing a large $\tau^+\tau^-$ generic MC sample. This effective description can generally discard information about correlations in the phase space and thereby give significant bias. The residuals of the fitted Michel parameters from the SM prediction obtained by the fit to the MC distribution are taken as the corresponding systematic uncertainties.

Table 3. List of systematic contributions.

Item	$\sigma_{\bar{\eta}}^e$	$\sigma_{\xi\kappa}^e$	$\sigma_{\bar{\eta}}^\mu$	$\sigma_{\xi\kappa}^\mu$	Evaluated by
Relative normalizations	3.8	0.69	0.13	0.04	MC
Absolute normalizations	1.0	0.01	0.03	0.001	MC
Formulation of PDFs	2.5	0.24	0.67	0.22	MC
Input of branching ratio	3.8	0.05	0.25	0.01	PDG value
Effect of cluster overlap in ECL	2.2	0.46	0.02	0.06	Data
Detector resolution	0.74	0.20	0.22	0.02	MC
Exp/MC corrections	1.9	0.14	0.09	0.10	Data
E_γ selection	0.91	0.22	—	—	Data
Total	6.8	0.93	0.77	0.25	

Table 4. Systematic uncertainties due to EXP/MC efficiency corrections.

Item	$\sigma_{\bar{\eta}}^e$	$\sigma_{\xi\kappa}^e$	$\sigma_{\bar{\eta}}^\mu$	$\sigma_{\xi\kappa}^\mu$
Trigger efficiency	0.5	0.10	0.04	0.03
ℓ ID efficiency	negligible	0.01	0.08	0.09
π ID efficiency	negligible	negligible	negligible	negligible
π^0 ID efficiency	0.4	0.09	negligible	0.01
γ efficiency	0.14	0.03	0.015	0.02
$(e\gamma, \pi\pi^0) + \gamma_{\text{brems}}$ inefficiency	1.8	0.04	—	—
Total	1.9	0.14	0.09	0.10

Other notable uncertainties come from the accuracy of the measured branching ratios. In particular, the uncertainties of the branching ratios of the radiative decay $\tau^- \rightarrow \ell^- \nu_\tau \bar{\nu}_\ell \gamma$ dominate. The systematic effects of the cluster merging in the ECL are evaluated as a function of the angle between the photon and lepton clusters at the inner surface of ECL ($\theta_{\ell\gamma}^{\text{ECL}}$). The limit $\theta_{\ell\gamma}^{\text{ECL}} \rightarrow 0$ represents the merger of the two clusters, and the comparison of the distribution between experiment and MC gives us the corresponding bias. A systematic effect due to the detector resolution is evaluated by comparing Michel parameters obtained in the fit with and without account of the resolution function.

The error of the measured correction factor R is estimated by varying the central values based on the uncertainty in each bin. Moreover, as can be observed in Fig. 8(d) in the muon mode, there is a notable disagreement of efficiency in the forward domain ($\cos\theta_\mu^{\text{LAB}} > 0.9$). This is due to the contamination of backgrounds in the extraction of the correction factor of $R_{\mu\text{ID}}$. We excluded this region (reducing the statistics by 1.5%) and checked the shift of the refitted Michel parameters. The uncertainty due to the forward background is taken into account as a systematic effect.

In the electron mode, we observe the disagreement of the photon reconstruction efficiency in the low-energy region—Fig. 8(e). It could arise from a discrepancy in the simulation of external bremsstrahlung. We excluded the events having a low-energy photon $E_\gamma^{\text{LAB}} < 150$ MeV and compared the refitted values. Because this requirement reduces the number of events by approximately 20%, the statistical fluctuation is also reflected in the shifts.

The effect of the beam-energy spread is estimated by varying the input of this value for the calculation of the PDF with respect to run-dependent uncertainties, and turns out to be negligible.

The effects from the next-to-leading-order (NLO) contribution were checked by adding the NLO formulae [31] to the signal PDF and refitting, and were found to be negligible.

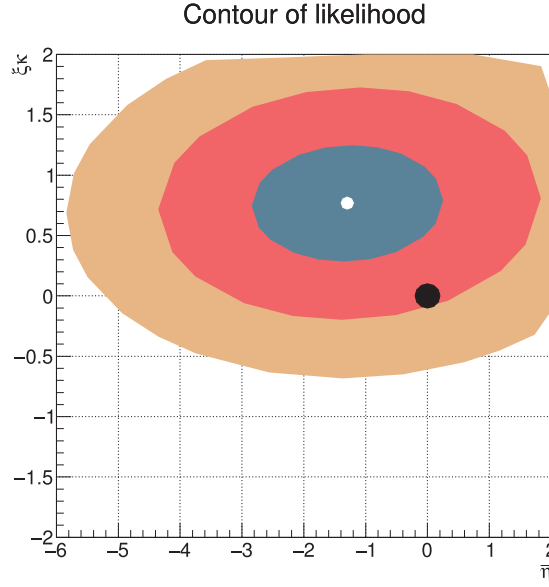


Fig. 9. Contours of the likelihood function obtained using 71171 events for $\tau^- \rightarrow \mu^- \nu_\tau \bar{\nu}_\mu \gamma$ candidates. The ovals are 1σ , 2σ , and 3σ contours of statistical deviation of the likelihood function from the best estimation. The black dot is the SM prediction.

6. Results

Because of the suppression of sensitivity due to the small mass of the electron, the $\bar{\eta}$ parameter is extracted only from the $\tau^- \rightarrow \mu^- \nu_\tau \bar{\nu}_\mu \gamma$ mode. Using the 71171 selected $\tau^- \rightarrow \mu^- \nu_\tau \bar{\nu}_\mu \gamma$ candidates, $\bar{\eta}$ and $\xi\kappa$ are simultaneously fitted to the kinematic distribution to be:

$$\bar{\eta}^\mu = -1.3 \pm 1.5(\text{stat}) \pm 0.8(\text{syst}), \quad (23)$$

$$(\xi\kappa)^\mu = 0.8 \pm 0.5(\text{stat}) \pm 0.3(\text{syst}). \quad (24)$$

Figure 9 shows the contour of the likelihood function for $\tau^- \rightarrow \mu^- \nu_\tau \bar{\nu}_\mu \gamma$ events.

In the electron mode, $\xi\kappa$ is fitted by fixing the $\bar{\eta}$ value to the SM prediction of $\bar{\eta} = 0$, and the best-fit value is extracted using 776834 events to be

$$(\xi\kappa)^e = -0.4 \pm 0.8(\text{stat}) \pm 0.9(\text{syst}). \quad (25)$$

The obtained values are consistent with the SM prediction.

Furthermore, the $\xi\kappa$ product is also obtained by fitting simultaneously to both electron and muon events ($\bar{\eta}$ is relaxed) as

$$\xi\kappa = 0.5 \pm 0.4(\text{stat}) \pm 0.2(\text{syst}). \quad (26)$$

Here, the systematic uncertainty is estimated from $1/\sigma_{\text{comb}}^2 = 1/\sigma_e^2 + 1/\sigma_\mu^2$ by assuming they are uncorrelated.

We also obtain the dependence of the fitted $\bar{\eta}$ and $\xi\kappa$ parameters on the different $E_{\text{extra}\gamma}^{\text{LAB}}$ cut values as shown in Fig. 10. In the extraction of $\bar{\eta}$ we use $\tau^- \rightarrow \mu^- \nu_\tau \bar{\nu}_\mu \gamma$, while for $\xi\kappa$ we use the combined result for the $\tau^- \rightarrow e^- \nu_\tau \bar{\nu}_e \gamma$ and $\tau^- \rightarrow \mu^- \nu_\tau \bar{\nu}_\mu \gamma$ decays. We observe stability of the fitted Michel parameters within the uncertainties. Figure 11 shows the residual of the likelihood function $\Delta L = \text{NLL}_{\text{min}} - \text{NLL}$ projected onto one axis. We observe a smooth, quadratic shape of the NLL around its minimum.

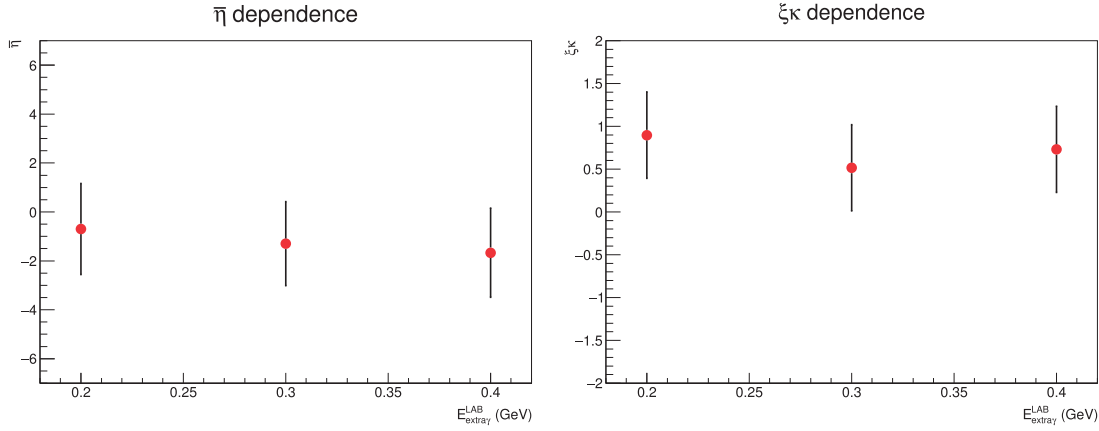


Fig. 10. Dependence of fitted Michel parameters on the different $E_{\text{extray}}^{\text{LAB}}$ cut values: (a) $\bar{\eta}$; (b) $\xi\kappa$. The red markers with bars correspond to the best-fit values of the Michel parameters and their uncertainties, where both statistical and systematic uncertainties are considered.

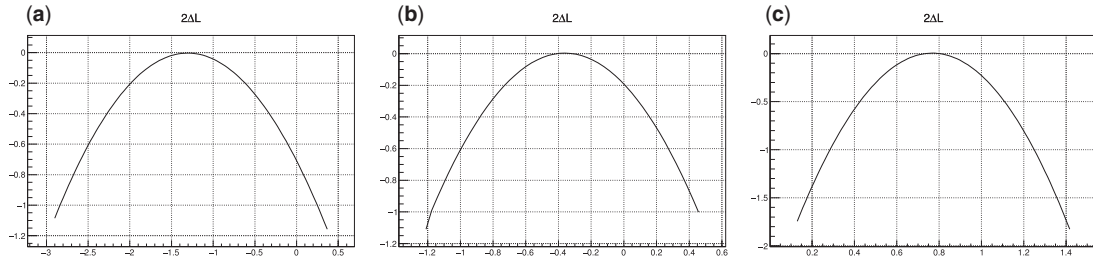


Fig. 11. Plot of $2 \times \Delta L$ as a function of the Michel parameters. (a) $-2\text{NLL}(\bar{\eta}^\mu)$ when $\xi\kappa$ is set to the fitted value. (b) $2\Delta L(\xi\kappa^e)$ when $\bar{\eta} = \bar{\eta}_{\text{SM}} = 0$. (c) $2\Delta L(\xi\kappa^\mu)$ when $\bar{\eta}$ is set to the fitted value.

7. Measurement of the branching ratio $\mathcal{B}(\tau^- \rightarrow \ell^- \nu_\tau \bar{\nu}_\ell \gamma)$

In addition to the Michel parameters, we have determined the branching ratios of the $\tau^- \rightarrow \ell^- \nu_\tau \bar{\nu}_\ell \gamma$ ($\ell = e, \mu$) decays.

Following the definition of Ref. [31], we distinguish between two types of radiative decays in the NLO approximation: exclusive radiative decay implies that only one hard photon is emitted in the event; in inclusive radiative decay, at least one hard photon is emitted. Here, the hard photon energy threshold is 10 MeV in the τ^- rest frame.

In Ref. [31], the precision measurement of the branching ratios of the radiative leptonic τ decays at BaBar is also discussed. While the measured branching ratios of both electron and muon modes agree with their leading-order (LO) theoretical predictions, the NLO exclusive branching ratio prediction for the $\tau^- \rightarrow e^- \nu_\tau \bar{\nu}_e \gamma$ decay differs from the BaBar result by 3.5 standard deviations. However, there is room for discussion. Since it is impossible to decisively veto an additional photon, particularly when the photon energy is small, the experimental branching ratio should not be interpreted as an ideal exclusive branching ratio even if one tries to reject the additional photon. It is, rather, reasonable to regard it as falling between the exclusive and inclusive branching ratios.

In other words, this discrepancy can be explained by the insufficient accuracy of the current MC simulation of the radiative and doubly radiative leptonic τ decays. Neither an NLO correction to the radiative leptonic decay, nor the doubly radiative leptonic mode itself, are incorporated in the current version of the TAUOLA MC generator. As a result, the detection efficiency is not precisely evaluated

for the radiative decay. Also, the background from the doubly radiative decay is not subtracted at all. Finally, the second photon emission might affect the efficiency of the photon veto and the shape of the neutral clusters in the calorimeter. Indeed, the ratio of the yield with two-photon emission to that with single-photon emission is approximately 5% and 1% for the electron and muon modes, respectively. Thus, there is an experimentally notable impact of the two-photon emission on the electron mode.

In our measurement of the branching ratios, we do not take into account the up-to-date formalism of Ref. [31] since the main purpose of this study is a consistency check of our selection criteria and experimental efficiency corrections.

7.1. Method

The branching ratio is determined using:

$$\mathcal{B}(\tau^- \rightarrow \ell^- \nu_\tau \bar{\nu}_\ell \gamma) = \frac{N_{\text{obs}}(1 - f_{\text{bg}})}{2\sigma_{\tau\tau} L \mathcal{B}(\tau^+ \rightarrow \pi^+ \pi^0 \bar{\nu}_\tau) \bar{\varepsilon}^{\text{EX}}}, \quad (27)$$

where $\mathcal{B}(\tau^+ \rightarrow \pi^+ \pi^0 \bar{\nu}_\tau) = (25.52 \pm 0.09)\%$ [11] is the branching ratio of $\tau^+ \rightarrow \pi^+ \pi^0 \bar{\nu}_\tau$ decay, N_{obs} is the number of observed events, f_{bg} is the fraction of background events, $\sigma_{\tau\tau} = (0.919 \pm 0.003)$ nb is the cross section of the $e^+e^- \rightarrow \tau^+\tau^-$ process at $\Upsilon(4S)$ [32], $L = (711 \pm 10)$ fb $^{-1}$ is the integrated luminosity recorded at $\Upsilon(4S)$, and $\bar{\varepsilon}^{\text{EX}}$ is the average detection efficiency of signal events. The efficiency, $\bar{\varepsilon}^{\text{EX}}$, is evaluated with help of the MC simulation. The correction factor, $R(\mathbf{x}) = \varepsilon^{\text{EX}}(\mathbf{x})/\varepsilon^{\text{MC}}(\mathbf{x})$, which is used to extract the Michel parameters, is applied to compensate for the difference between experimental and MC efficiencies as follows:

$$\begin{aligned} \bar{\varepsilon}^{\text{EX}} &= \frac{1}{N_0} \int d\mathbf{x} \mathcal{S}_0(\mathbf{x}) \varepsilon^{\text{EX}}(\mathbf{x}) = \frac{1}{N_0} \int d\mathbf{x} \mathcal{S}_0(\mathbf{x}) \varepsilon^{\text{MC}}(\mathbf{x}) R(\mathbf{x}) \\ &= \frac{\bar{\varepsilon}^{\text{MC}}}{N_{\text{sel}}} \sum_{i:\text{sel}(\text{MC})} R(\mathbf{x}^i) = \bar{\varepsilon}^{\text{MC}} \bar{R}, \end{aligned} \quad (28)$$

where $\mathcal{S}_0(\mathbf{x})$ is the SM PDF of the signal events and \bar{R} is an average efficiency correction factor for the selected signal MC events. Here, the average MC efficiency, $\bar{\varepsilon}^{\text{MC}}$, is determined for the photon energy threshold of 10 MeV in the τ rest frame.

7.2. Event selection

We apply additional selection criteria to enhance the purity of the sample as well as to reduce systematic uncertainties. The extra-gamma-energy selection is released for the latter purpose, but other selection criteria are common to those of Michel parameter measurement (see Sect. 3).

For the electron mode, we apply the following selection criteria:

- The uncertainty of the lepton identification efficiency in the forward and backward regions of the detector is large due to the notable background contamination of the control sample; thus, the electron polar angle in the laboratory frame must lie in the region defined by $\theta_e^{\text{LAB}} < 126^\circ$, as shown in Fig. 12(a).
- The electron identification is less precise at small momenta, so we apply the momentum threshold $P_e^{\text{LAB}} > 1.5$ GeV/ c as shown in Fig. 12(c).
- After the final selections (explained in Sect. 3), the dominant background arises from the external bremsstrahlung on the material of the detector. It is effectively suppressed by applying the

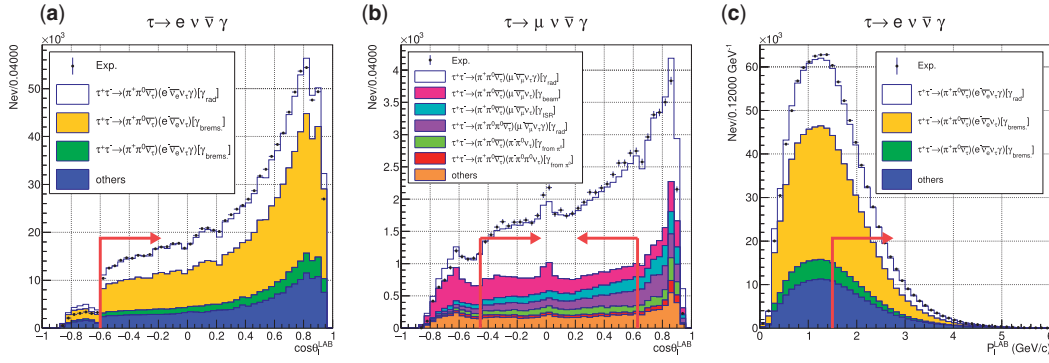


Fig. 12. Cosine of the polar angle for the electron (a) and muon (b) modes, and momentum of electron (c). The color of each histogram is explained in the caption of Fig. 3, and the red arrows indicate the selection windows: (a) $\theta_e^{\text{LAB}} < 126^\circ$, (b) $51^\circ < \theta_\mu^{\text{LAB}} < 117^\circ$, and (c) $P_e^{\text{LAB}} > 1.5 \text{ GeV}/c$. The relative drops in the efficiencies are approximately 2%, 50%, and 36% for (a), (b), and (c), respectively. The small peak around $\theta_{\text{LAB}} \sim 90^\circ$ seen in (b) comes from the beam background.

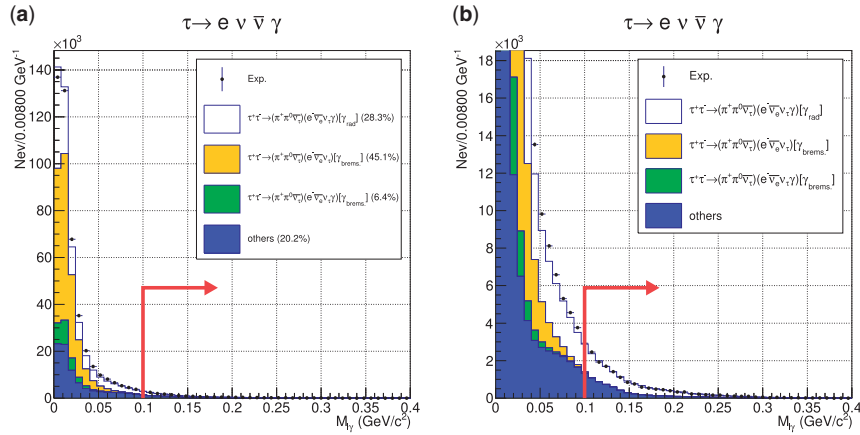


Fig. 13. Distribution of the invariant mass of $e\text{-}\gamma$ system, $M_{e\gamma}$. The color of each histogram is explained in Fig. 3, and the red arrows indicate the selection windows. (a) Overall view; (b) enlarged view. The relative decrease of the efficiency is 93%.

requirement on the invariant mass of the electron–photon system, $M_{e\gamma} > 0.1 \text{ GeV}/c^2$, as shown in Fig. 13.

- The extra gamma energy in the laboratory frame, $E_{\text{extra}\gamma}^{\text{LAB}}$, must be less than 0.2 GeV.

For the muon mode, we apply the following selection criteria:

- The muon polar angle in the laboratory frame must satisfy $51^\circ < \theta_\mu^{\text{LAB}} < 117^\circ$, as shown in Fig. 12(b).
- The spatial angle between μ and γ in c.m.s. must satisfy $\cos\theta_{\mu\gamma} > 0.99$.
- The extra gamma energy in laboratory frame, $E_{\text{extra}\gamma}^{\text{LAB}}$, must be smaller than 0.3 GeV.

7.3. Evaluation of systematic uncertainties

In Table 5, we summarize the sources of the systematic uncertainties of the branching ratios of the electron and muon modes. To estimate a systematic uncertainty from the efficiency correction, \bar{R} , we use the following method. The uncertainties of the R_{fid} are determined by the finite statistics of

Table 5. Systematic uncertainties (%) on $\mathcal{B}(\tau^- \rightarrow \ell^- \nu_\tau \bar{\nu}_\ell \gamma)$ for different configurations.

Item	$(e^- \gamma, \pi^+ \pi^0)$	$(e^+ \gamma, \pi^- \pi^0)$	$(\mu^- \gamma, \pi^+ \pi^0)$	$(\mu^+ \gamma, \pi^- \pi^0)$
$R_{\ell\text{ID}}$	1.9	1.9	1.1	1.1
$R_{\pi\text{ID}}$	0.7	0.7	0.7	0.7
$R_{\gamma\text{ID}}$	1.0	1.0	0.4	0.4
$R_{\pi^0\text{ID}}$	3.6	3.6	3.3	3.3
R_{trg}	1.2	1.2	0.7	0.7
R_{trk}	0.7	0.7	0.7	0.7
Purity ($1 - f_{\text{bg}}$)	1.3	1.3	1.5	1.5
Detector response	1.5	1.5	0.6	0.6
Uncertainty of E_γ^* threshold	1.1	1.1	0.3	0.3
Luminosity	1.4	1.4	1.4	1.4
$\mathcal{B}(\tau^+ \rightarrow \pi^+ \pi^0 \nu)$	0.4	0.4	0.4	0.4
$\sigma(e^+ e^- \rightarrow \tau^+ \tau^-)$	0.3	0.3	0.3	0.3
Total	5.3	5.3	4.3	4.3

the $e^+ e^- \rightarrow e^+ e^- \ell^+ \ell^-$ sample, a comparison of $R_{\ell\text{ID}}$ from $e^+ e^- \rightarrow e^+ e^- \ell^+ \ell^-$ and $R_{\ell\text{ID}}$ from $J/\psi \rightarrow \ell^+ \ell^-$, and its time variation during the experiment.

$R_{\pi\text{ID}}$ values are estimated from the finite statistics of a $D^{*+} \rightarrow D^0(K^- \pi^+) \pi^+$ sample, the fit of the reconstructed mass distribution of D^* , and observation of time variation.

The systematic uncertainties of the $R_{\pi^0\text{ID}}$, $R_{\gamma\text{ID}}$, R_{trg} , and R_{trk} values are estimated from a comparison between \bar{R} and unity.

The uncertainty of $\mathcal{B}(\tau^+ \rightarrow \pi^+ \pi^0 \bar{\nu}_\tau)$ is taken from the PDG average value [11], and that of $\sigma(e^+ e^- \rightarrow \tau^+ \tau^-)$ is taken from Ref. [32].

The statistical uncertainty of MC events is ignored because its effect is small.

The evaluation of the systematic uncertainty of the purity $1 - f_{\text{bg}}$ is estimated based on sideband information. The sideband events are selected by the following criteria: $M_{e\gamma} < 0.1 \text{ GeV}/c^2$ and $0.90 < \cos\theta_{e\gamma} < 0.94$ for the electron mode and $0.90 < \cos\theta_{\mu\gamma} < 0.99$ for the muon mode, where other selection criteria are common with those of the signal extraction. The difference of the background yield in the sideband region between MC simulation and the real experiment is 4.4% (5.5%) for the electron (muon) mode. Taking each fraction into account, we estimate that the resulting uncertainty is 1.3% and 1.5%.

The effect of detector response is estimated by varying selection parameters. The effect due to variation of the photon energy threshold is based on the energy resolution at the threshold, and found to be 5% [21,22]. The variation of other selection criteria are determined based on the CDC angular and momentum resolutions for the charged particles. Of all the selection criteria, the requirement of $M_{e\gamma} > 0.1 \text{ GeV}/c^2$ has the largest impact.

As mentioned, to estimate the efficiency, we define the radiative events by the imposition of a photon energy threshold of $E_\gamma^* = 10 \text{ MeV}$ in the τ^- rest frame. However, in the real experiment, we cannot precisely determine this energy because the τ^- momentum is not directly reconstructed. Accordingly, there is a chance that an event that has a photon with an energy less than the threshold is also reconstructed as signal. This is only possible in a limited phase space, and such events are included in the selection with the fractions of 1.1% and 0.3% for electron and muon events, respectively. We take these fractions as sources of systematic effects due to the uncertainty of the experimental E_γ^* threshold.

Table 6. Summary of results for the branching ratio measurement. The first and second errors of the branching ratio \mathcal{B} are the statistical and systematic uncertainties.

Item	$(e^- \gamma, \pi^+ \pi^0)$	$(e^+ \gamma, \pi^- \pi^0)$	$(\mu^- \gamma, \pi^+ \pi^0)$	$(\mu^+ \gamma, \pi^- \pi^0)$
N_{obs}	6188 ± 79	6114 ± 78	10458 ± 102	11170 ± 106
$1 - f_{\text{bg}}$ (%)	70.2 ± 0.9	70.2 ± 0.9	71.5 ± 1.0	71.5 ± 1.0
$\bar{\varepsilon}^{\text{MC}}$ (%)	0.172 ± 0.001	0.169 ± 0.001	1.26 ± 0.01	1.27 ± 0.01
\bar{R}	0.85 ± 0.04	0.85 ± 0.04	0.93 ± 0.03	0.93 ± 0.03
$\bar{\varepsilon}^{\text{EX}}$ (%)	0.146 ± 0.007	0.144 ± 0.007	1.28 ± 0.05	1.29 ± 0.05
\mathcal{B} (%)	$1.79 \pm 0.02 \pm 0.09$	$1.80 \pm 0.02 \pm 0.10$	$0.352 \pm 0.003 \pm 0.015$	$0.373 \pm 0.003 \pm 0.016$

Table 7. Information on the branching ratios of the radiative leptonic τ decays.

	$\tau^- \rightarrow e^- \nu_\tau \bar{\nu}_e \gamma$	$\tau^- \rightarrow \mu^- \nu_\tau \bar{\nu}_\mu \gamma$
This measurement	$(1.79 \pm 0.02 \pm 0.10) \times 10^{-2}$	$(3.63 \pm 0.02 \pm 0.15) \times 10^{-3}$
BaBar (experiment; [33])	$(1.847 \pm 0.015 \pm 0.052) \times 10^{-2}$	$(3.69 \pm 0.03 \pm 0.10) \times 10^{-3}$
CLEO (experiment; [34])	$(1.75 \pm 0.06 \pm 0.017) \times 10^{-2}$	$(3.61 \pm 0.16 \pm 0.35) \times 10^{-3}$
LO (theory; [31])	1.834×10^{-2}	3.663×10^{-3}
NLO inclusive (theory; [31])	1.728×10^{-2}	3.605×10^{-3}
NLO exclusive (theory; [31])	1.645×10^{-2}	3.572×10^{-3}

7.4. Result

In Table 6, we show the result of the measurement separately for the four configurations $(e^- \gamma, \pi^+ \pi^0)$, $(e^+ \gamma, \pi^- \pi^0)$, $(\mu^- \gamma, \pi^+ \pi^0)$, and $(\mu^+ \gamma, \pi^- \pi^0)$. They are combined to give:

$$\mathcal{B}(\tau^- \rightarrow e^- \nu_\tau \bar{\nu}_e \gamma)_{E_\gamma^* > 10 \text{ MeV}} = (1.79 \pm 0.02 \pm 0.09) \times 10^{-2}, \quad (29)$$

$$\mathcal{B}(\tau^- \rightarrow \mu^- \nu_\tau \bar{\nu}_\mu \gamma)_{E_\gamma^* > 10 \text{ MeV}} = (3.63 \pm 0.02 \pm 0.15) \times 10^{-3}, \quad (30)$$

where the first error is statistical and the second is systematic. In Table 7, we summarize the current experimental and theoretical information on these decays. While the LO theoretical calculations for these decays were done a long time ago, NLO corrections were considered thoroughly only recently in Ref. [31], where the importance of taking into account the hard doubly radiative decays was emphasized.

We also obtain the dependence of branching ratio on the $E_{\text{extra}\gamma}^{\text{LAB}}$ selection, as shown in Fig. 14. These results are consistent with the LO theoretical prediction.

As summarized in Table 5, the dominant contribution to the systematic uncertainty comes from the π^0 efficiency correction. This uncertainty is canceled when we measure the ratio of branching fractions $\mathcal{Q} = \mathcal{B}(\tau^- \rightarrow e^- \nu_\tau \bar{\nu}_e \gamma) / \mathcal{B}(\tau^- \rightarrow \mu^- \nu_\tau \bar{\nu}_\mu \gamma)$. Moreover, other common systematic sources, namely R_{trk} , $R_{\pi\text{ID}}$, the integrated luminosity, the branching ratio of $\tau^+ \rightarrow \pi^+ \pi^0 \bar{\nu}_\tau$ decays, and the cross section $\sigma(e^+ e^- \rightarrow \tau^+ \tau^-)$, also cancel. The obtained ratio is

$$\mathcal{Q} = \frac{\mathcal{B}(\tau^- \rightarrow e^- \nu_\tau \bar{\nu}_e \gamma)_{E_\gamma^* > 10 \text{ MeV}}}{\mathcal{B}(\tau^- \rightarrow \mu^- \nu_\tau \bar{\nu}_\mu \gamma)_{E_\gamma^* > 10 \text{ MeV}}} = 4.95 \pm 0.06 \pm 0.20, \quad (31)$$

where the first error is statistical and the second is systematic. In Table 8, we summarize the theoretical prediction and past experimental results for the ratio \mathcal{Q} .

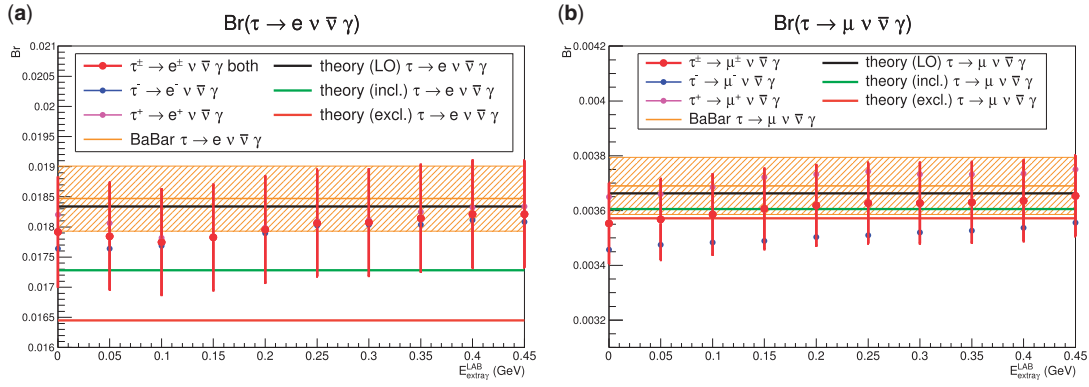


Fig. 14. Branching ratio of $\tau^- \rightarrow \ell^- \nu_\tau \bar{\nu}_\ell \gamma$ decay as a function of the $E_{\text{extray}}^{\text{LAB}}$ cut: (a) $\ell = e$; (b) $\ell = \mu$. The red, blue, and magenta lines represent the measured branching ratio of $\tau^\pm \rightarrow \ell^\pm \nu \bar{\nu} \gamma$, $\tau^- \rightarrow \ell^- \nu_\tau \bar{\nu}_\ell \gamma$, and $\tau^+ \rightarrow \ell^+ \nu_\ell \bar{\nu}_\tau \gamma$, respectively. The bars represent uncertainties and are drawn only for the combined modes, where both statistical and systematic uncertainties are included. The orange band shows the BaBar measurement [33]. The black, green, and red lines are the LO, NLO inclusive, and NLO exclusive theoretical predictions, respectively [31].

Table 8. Comparison of the ratio Q ($E_\gamma^* > 10$ MeV).

Theory	
Leading order	5.007
Next-to-leading order incl.	4.793
Next-to-leading order excl.	4.605
Experiment	
CLEO	4.9 ± 0.6 [34]
BaBar	$5.01 \pm 0.20^*$ [33]
This measurement	$4.95 \pm 0.06 \pm 0.20$

*Systematic uncertainty is calculated from the reference values, where cancellation is not taken into account. The statistical and systematic uncertainties are combined for the CLEO and BaBar measurements.

8. Conclusion

We present the measurement of Michel parameters $\bar{\eta}$ and $\xi\kappa$ of the τ using 711 fb^{-1} of data collected with the Belle detector at the KEKB e^+e^- collider. These parameters are extracted from the radiative leptonic decay $\tau^- \rightarrow \ell^- \nu_\tau \bar{\nu}_\ell \gamma$ which is tagged by $\tau^+ \rightarrow \rho^+(\rightarrow \pi^+\pi^0)\bar{\nu}_\tau$ decay of the partner τ^+ to exploit the spin–spin correlation in $e^+e^- \rightarrow \tau^+\tau^-$. Due to the small sensitivity to $\bar{\eta}$ in the electron mode, this parameter is extracted only from $\tau^- \rightarrow \mu^- \nu_\tau \bar{\nu}_\mu \gamma$ to give $\bar{\eta} = -1.3 \pm 1.5 \pm 0.8$. The product $\xi\kappa$ is measured using both decays $\tau^- \rightarrow \ell^- \nu_\tau \bar{\nu}_\ell \gamma$ ($\ell = e$ and μ) to be $\xi\kappa = 0.5 \pm 0.4 \pm 0.2$. The first error is statistical and the second is systematic. This is the first measurement of both parameters for the τ lepton. These values are consistent with the SM expectation within the uncertainties.

For a consistency check of the procedure to measure the Michel parameters, we measure the branching ratio of the $\tau^- \rightarrow \ell^- \nu_\tau \bar{\nu}_\ell \gamma$ decay. The obtained values are consistent with the LO theoretical prediction and support the measurement by BaBar, which is known to deviate from the SM exclusive branching ratio by 3.5σ . Accounting for the agreement between our result and the

BaBar measurement [33], the implementation of the NLO formalism in the TAUOLA generator is required to carry out more precise measurements.

Acknowledgements

We would like to express our deepest appreciation to A. Arbuzov, M. Fael, T. Kopylova, L. Mercolli, and M. Passera for very useful discussions and theoretical support of this work. We thank the KEKB group for the excellent operation of the accelerator; the KEK cryogenics group for the efficient operation of the solenoid; and the KEK computer group, the National Institute of Informatics, and the PNNL/EMSL computing group for valuable computing and SINET5 network support. We acknowledge support from the Ministry of Education, Culture, Sports, Science, and Technology (MEXT) of Japan, the Japan Society for the Promotion of Science (JSPS), and the Tau-Lepton Physics Research Center of Nagoya University; the Australian Research Council; the Austrian Science Fund under Grant No. P 26794-N20; the National Natural Science Foundation of China under Contracts No. 10575109, No. 10775142, No. 10875115, No. 11175187, No. 11475187, No. 11521505, and No. 11575017; the Chinese Academy of Science Center for Excellence in Particle Physics; the Ministry of Education, Youth and Sports of the Czech Republic under Contract No. LTT17020; the Carl Zeiss Foundation, the Deutsche Forschungsgemeinschaft, the Excellence Cluster Universe, and the VolkswagenStiftung; the Department of Science and Technology of India; the Istituto Nazionale di Fisica Nucleare of Italy; the WCU program of the Ministry of Education, National Research Foundation (NRF) of Korea Grants No. 2011-0029457, No. 2012-0008143, No. 2014R1A2A2A01005286, No. 2014R1A2A2A01002734, No. 2015R1A2A2A01003280, No. 2015H1A2A1033649, No. 2016R1D1A1B01010135, No. 2016K1A3A7A09005603, No. 2016K1A3A7A09005604, No. 2016R1D1A1B02012900, No. 2016K1A3A7A09005606, and No. NRF-2013K1A3A7A06056592; the Brain Korea 21-Plus program, Radiation Science Research Institute, Foreign Large-size Research Facility Application Supporting project, and the Global Science Experimental Data Hub Center of the Korea Institute of Science and Technology Information; the Polish Ministry of Science and Higher Education and the National Science Center; the Ministry of Education and Science of the Russian Federation and the Russian Foundation for Basic Research, grant 15-02-05674; the Slovenian Research Agency; Ikerbasque, Basque Foundation for Science and MINECO (Juan de la Cierva), Spain; the Swiss National Science Foundation; the Ministry of Education and the Ministry of Science and Technology of Taiwan; and the U.S. Department of Energy and the National Science Foundation.

Funding

Open Access funding: SCOAP³.

Appendix A. Differential decay width of $\tau^- \rightarrow \ell^- \nu_\tau \bar{\nu}_\ell \gamma$

The differential cross section of $\tau^- \rightarrow \ell^- \nu_\tau \bar{\nu}_\ell \gamma$ decay is expressed as a sum of two terms:

$$\frac{d\Gamma(\tau^\mp \rightarrow \ell^\mp \nu_\tau \bar{\nu}_\ell \gamma)}{dE_\ell^* d\Omega_\ell^* dE_\gamma^* d\Omega_\gamma^*} = A \mp \mathbf{B} \cdot \mathbf{S}_{\tau^\mp}, \quad (\text{A1})$$

where A and \mathbf{B} represent spin-independent and spin-dependent terms, E_i^* ($i = \ell, \gamma$) is the energy in the τ rest frame, and Ω_i ($i = \ell, \gamma$) is the solid angle defined by $\{\cos\theta_i, \phi_i\}$ ($i = \ell, \gamma$). These terms are functions of dimensionless kinematic parameters x , y , and d defined as:

$$r = \frac{m_\ell}{m_\tau}, \quad (\text{A2})$$

$$x = \frac{2E_\ell^*}{m_\tau} \quad (2r < x < 1 + r^2), \quad (\text{A3})$$

$$y = \frac{2E_\gamma^*}{m_\tau} \quad (0 < y < 1 - r), \quad (\text{A4})$$

$$d = 1 - \beta_\ell^* \cos \theta_{\ell\gamma}^*, \quad (\text{A5})$$

$$y < \frac{2(1 + r^2 - x)}{2 - x + \cos \theta_{\ell\gamma}^* \sqrt{x^2 - 4r^2}}, \quad (\text{A6})$$

where $\theta_{\ell\gamma}^*$ is the angle between the daughter lepton and the photon, and β_ℓ^* is the velocity of the daughter lepton in the τ rest frame; A and B are parametrized by the Michel parameters ρ , η , ξ , $\xi\delta$, $\bar{\eta}$, η'' , and $\xi\kappa$.

$$A(x, y, d) = \frac{4\alpha G_F^2 m_\tau^3}{3(4\pi)^6} \cdot \beta_\ell^* \sum_{i=0,1,\dots,5} F_i r^i, \quad (\text{A7})$$

$$B(x, y, d) = \frac{4\alpha G_F^2 m_\tau^3}{3(4\pi)^6} \cdot \beta_\ell^* \sum_{i=0,1,\dots,5} (\beta_l^* G_i \mathbf{n}_l^* + H_i \mathbf{n}_\gamma^*) r^i, \quad (\text{A8})$$

where \mathbf{n}_l^* and \mathbf{n}_γ^* are the normalized directions of the lepton and photon in the τ rest frame, respectively. The F_i , G_i , and H_i ($i = 0, 1, \dots, 5$) are functions of x , y , d , and r , and their explicit formulae are given in the Appendix of Ref. [7].

Appendix B. Differential decay width of $\tau \rightarrow \rho \nu_\tau$

The differential decay width of the $\tau^\pm \rightarrow \rho^\pm \nu_\tau$ decay is expressed as a sum of the spin-independent and spin-dependent parts:

$$\frac{d\Gamma(\tau^\pm \rightarrow \pi^\pm \pi^0 \nu_\tau)}{d\Omega_\rho^* dm^2 d\tilde{\Omega}_\pi} = A^\pm \mp \xi_\rho \mathbf{B}^\pm \cdot \mathbf{S}_{\tau^\pm}, \quad (\text{B1})$$

$$A^+ = \frac{G_F^2 |V_{ud}|^2}{(4\pi)^5} \cdot [2(E_\pi^* - E_{\pi^0}^*)(p_\nu \cdot q) - E_\nu^{*2} q^2] \cdot \text{BPS}, \quad (\text{B2})$$

$$\mathbf{B}^+ = \frac{G_F^2 |V_{ud}|^2}{(4\pi)^5} \cdot [\mathbf{P}_\pi^* \{(q \cdot q) + 2(p_\nu \cdot q)\} + \mathbf{P}_{\pi^0}^* \{(q \cdot q) - 2(p_\nu \cdot q)\}] \cdot \text{BPS}, \quad (\text{B3})$$

where V_{ud} is the corresponding element of the Cabibbo–Kobayashi–Maskawa matrix, E_i^* and \mathbf{P}_i^* ($i = \pi, \pi^0$) are the energies and three-momenta measured in the τ rest frame, Ω_ρ^* is the solid angle of the ρ meson in the τ rest frame, $\tilde{\Omega}_\pi$ is the solid angle of the pion in the ρ rest frame, q is a four-momentum defined by $q = p_\pi - p_{\pi^0}$, and p_ν is the four-momentum of the τ neutrino. The factor BPS stands for the square of a relativistic Breit–Wigner function and a Lorentz-invariant phase space:

$$\text{BPS} = |F(m^2)|^2 \left(\frac{2P_\rho^*(m^2)}{m_\tau} \right) \left(\frac{2\tilde{P}_\pi(m^2)}{m_\rho} \right), \quad F(m^2) = \frac{F_\rho + \beta F_{\rho'}}{1 + \beta}, \quad (\text{B4})$$

$$F_\rho(m^2) = \frac{m_{\rho^0}^2}{m_{\rho^0}^2 - m^2 - im_{\rho^0}\Gamma_\rho(m^2)}, \quad \Gamma_\rho(m^2) = \Gamma_{\rho^0} \frac{m_{\rho^0}}{\sqrt{m^2}} \left(\frac{\tilde{P}_\pi(m^2)}{\tilde{P}_\pi(m_{\rho^0}^2)} \right)^3, \quad (\text{B5})$$

$$F_{\rho'}(m^2) = \frac{m_{\rho'^0}^2}{m_{\rho'^0}^2 - m^2 - im_{\rho'^0}\Gamma_{\rho'}(m^2)}, \quad \Gamma_{\rho'}(m^2) = \Gamma_{\rho'^0} \frac{m_{\rho'^0}}{\sqrt{m^2}} \left(\frac{\tilde{P}_\pi(m^2)}{\tilde{P}_\pi(m_{\rho'^0}^2)} \right)^3, \quad (\text{B6})$$

$$\tilde{P}_\rho^*(m^2) = \frac{m_\tau^2 - m^2}{2m_\tau}, \quad (\text{B7})$$

$$\tilde{P}_\pi(m^2) = \frac{\sqrt{[m^2 - (m_\pi - m_{\pi^0})^2][m^2 - (m_\pi + m_{\pi^0})^2]}}{2m}. \quad (\text{B8})$$

We use the CLEO parametrization in the Breit–Wigner function, F_a ($a = \rho$ or ρ'), where the ρ and ρ' resonances are fixed at Ref. [13]:

$$m_{\rho^0} = 0.77 \text{ GeV}/c^2, \quad m_{\rho'^0} = 1.37 \text{ GeV}/c^2, \quad \Gamma_{\rho^0} = 0.151 \text{ GeV}, \quad \Gamma_{\rho'^0} = 0.51 \text{ GeV}. \quad (\text{B9})$$

The admixture of the ρ' state (β) is fixed at $\beta = -0.11$.

References

- [1] L. Michel, Proc. Phys. Soc. A **63**, 514 (1950).
- [2] C. Bouchiat and L. Michel, Phys. Rev. **106**, 170 (1957).
- [3] W. Fetscher, H.-J. Gerber, and K. F. Johnson, Phys. Lett. B **173**, 102 (1986).
- [4] W. Fetscher and H.-J. Gerber, Adv. Ser. Direct. High Energy Phys. **14**, 657 (1995).
- [5] M. Fael, L. Mercolli, and M. Passera, Phys. Rev. D **88**, 093011 (2013).
- [6] C. Fronsdal and H. Überall, Phys. Rev. **113**, 654 (1959).
- [7] A. B. Arbuzov and T. V. Kopylova, J. High Energy Phys. **09**, 109 (2016).
- [8] Y.-S. Tsai, Phys. Rev. D **4**, 2821 (1971); **13**, 771 (1976) [erratum].
- [9] W. Fetscher and H. J. Gerber, ETH-IMP PR-93-1 (1993).
- [10] A. Stahl and H. Voss, Z. Phys. C **74**, 73 (1997).
- [11] K.A. Olive et al. (Particle Data Group), Chin. Phys. C **38**, 090001 (2014).
- [12] A. Heister et al. (ALEPH Collaboration), Eur. Phys. J. C **22**, 217 (2001).
- [13] J. P. Alexander et al. (CLEO Collaboration), Phys. Rev. D **56**, 5320 (1997).
- [14] A. B. Arbuzov, E. A. Kuraev, G. V. Fedotovich, N. P. Merenkov, V. D. Rushai, and L. Trentadue, J. High Energy Phys. **10**, 001 (1997).
- [15] E. A. Kuraev and V. S. Fadin, Sov. J. Nucl. Phys. **41**, 466 (1985), [Yad. Fiz. **41** 733 (1985)].
- [16] F. A. Berends, R. Kleiss, S. Jadach, and Z. Was, Acta Phys. Polon. B **14**, 413 (1983).
- [17] S. Jadach and Z. Was, Acta Phys. Polon. B **15**, 1151 (1984); **16**, 483 (1985) [erratum].
- [18] S. Jadach and Z. Was, Comput. Phys. Commun. **36**, 191 (1985).
- [19] S. Kurokawa and E. Kikutani, Nucl. Instrum. Methods Phys. Res. Sect. A **499**, 1 (2003).
- [20] Y. Ohnishi et al., Prog. Theor. Exp. Phys. **2013**, 03A001 (2013).
- [21] A. Abashian et al. (Belle Collaboration), Nucl. Instrum. Methods Phys. Res. Sect. A **479**, 117 (2002).
- [22] J. Brodzicka et al., Prog. Theor. Exp. Phys. **2012**, 04D001 (2012).
- [23] K. Hanagaki, H. Kakuno, H. Ikeda, T. Iijima, and T. Tsukamoto, Nucl. Instrum. Meth. A **485**, 490 (2002).
- [24] A. Abashian et al., Nucl. Instrum. Meth. A **491**, 69 (2002).
- [25] B. G. Cheon et al., Nucl. Instrum. Meth. A **494**, 548 (2002).
- [26] Y. Ushiroda, A. Mohapatra, H. Sakamoto, Y. Sakai, M. Nakao, Q. An, and Y. F. Wang, Nucl. Instrum. Meth. A **438**, 460 (1999).
- [27] S. Jadach, B. F. L. Ward, and Z. Was, Comput. Phys. Commun. **130**, 260 (2000).
- [28] Z. Was, Nucl. Phys. Proc. Suppl. **98**, 96 (2001).
- [29] S. Jadach, Z. Was, R. Decker, and J. H. Kühn, Comput. Phys. Commun. **76**, 361 (1993).
- [30] R. Brun, R. Hagelberg, M. Hansroul, and J. C. Lassalle, CERN-DD-78-2 (1978).
- [31] M. Fael, L. Mercolli, and M. Passera, J. High Energy Phys. **07**, 153 (2015).
- [32] S. Banerjee, B. Pietrzyk, J. Michael Roney, and Z. Was, Phys. Rev. D **77**, 054012 (2008).
- [33] J. P. Lees et al. (BaBar Collaboration), Phys. Rev. D **91**, 051103(R) (2015).
- [34] T. Bergfeld et al. (CLEO Collaboration), Phys. Rev. Lett. **84**, 830 (2000).